

# Structure of subfilter-scale fluxes in the atmospheric surface layer with application to large-eddy simulation modelling

By PETER P. SULLIVAN<sup>1</sup>, THOMAS W. HORST<sup>1</sup>,  
DONALD H. LENSCHOW<sup>1</sup>, CHIN-HOH MOENG<sup>1</sup>,  
AND JEFFREY C. WEIL<sup>2</sup>

<sup>1</sup>National Center for Atmospheric Research, Boulder, CO 80307, USA

<sup>2</sup>CIRES, University of Colorado, Boulder, CO 80309, USA

(Received 15 July 2002 and in revised form 3 December 2002)

In the atmospheric surface layer, the wavelength of the peak in the vertical velocity spectrum  $\Lambda_w$  decreases with increasing stable stratification and proximity to the surface and this dependence constrains our ability to perform high-Reynolds-number large-eddy simulation (LES). Near the ground, the LES filter cutoff  $\Delta_f$  is comparable to or larger than  $\Lambda_w$  and as a result the subfilter-scale (SFS) fluxes in LES are always significant and their contribution to the total flux grows with increasing stability.

We use the three-dimensional turbulence data collected during the Horizontal Array Turbulence Study (HATS) field program to construct SFS fluxes and variances that are modelled in LES codes. Detailed analysis of the measured SFS motions shows that the ratio  $\Lambda_w/\Delta_f$  contains the essential information about stratification, vertical distance above the surface, and filter size, and this ratio allows us to connect measurements of SFS variables with LES applications. We find that the SFS fluxes and variances collapse reasonably well for atmospheric conditions and filter widths in the range  $\Lambda_w/\Delta_f = [0.2, 15]$ . The SFS variances are anisotropic and the SFS energy is non-inertial, exhibiting a strong dependence on the stratification, large-scale shear, and proximity to the surface. SFS flux decomposition into modified-Leonard, cross-, and Reynolds terms illustrates that these terms are of comparable magnitude and scale content at large  $\Lambda_w/\Delta_f$ . As  $\Lambda_w/\Delta_f \rightarrow 0$ , the SFS flux approaches the-ensemble-average flux and is dominated by the Reynolds term. Backscatter of energy from the SFS motions to the resolved fields is small in the bulk of the surface layer, less than 20% for  $\Lambda_w/\Delta_f < 2$ .

*A priori* testing of typical SFS models using the HATS dataset shows that the turbulent kinetic energy and Smagorinsky model coefficients  $C_k$  and  $C_s$  depend on  $\Lambda_w/\Delta_f$  and are smaller than theoretical estimates based on the assumption of a sharp spectral cutoff filter in the inertial range.  $C_k$  and  $C_s$  approach zero for small  $\Lambda_w/\Delta_f$ . Much higher correlations between measured and modelled SFS fluxes are obtained with a mixed SFS model that explicitly includes the modified-Leonard term. The eddy-viscosity model coefficients still retain a significant dependence on  $\Lambda_w/\Delta_f$  with the mixed model. A dissipation model of the form  $\epsilon = C_\epsilon E_s^{3/2}/\Delta_f$  is not universal across the range of  $\Lambda_w/\Delta_f$  typical of atmospheric LES applications. The inclusion of a shear-stability-dependent length scale (Canuto & Cheng 1997) captures a large fraction of the variation in the eddy-viscosity and dissipation model coefficients.

---

## 1. Introduction

Large-eddy simulation (LES) is a powerful tool for computing three-dimensional, time-dependent turbulent flows in geophysical and engineering sciences. However, in order for LES to attain widespread use as a computational method for high-Reynolds-number flows, advances on several fronts are required, e.g. general flow solvers, grid generation for complex geometry, specification of inflow and outflow boundary conditions, and of particular interest here, improved modelling of subfilter-scale (SFS) motions. In well-resolved regions of a turbulent flow the SFS motions are small and LES solutions are generally insensitive to the details of the SFS model. However, in flows with laminar-to-turbulent transition, strong stable stratification, or near solid boundaries, the SFS motions can become large and their impact on LES solutions is generally poorly understood.

The present work examines the specific problem of SFS turbulence modelling in the surface layer of the atmospheric planetary boundary layer (PBL). Surface-layer turbulence is strongly influenced by stratification, shear, and the presence of a rough boundary (Kaimal & Finnigan 1994). Previous studies (e.g. Mason & Thomson 1992; Sullivan, McWilliams & Moeng 1994; Saiki, Moeng & Sullivan 2000; Khana & Brasseur 1997; Stevens, Moeng & Sullivan 1999; and Zhou, Brasseur & Juneja 2001) provide evidence that LES solutions of the PBL are SFS model dependent to varying degrees, but less so for PBLs with vigorous unstable buoyancy forcing (Nieuwstadt *et al.* 1993).

Most LES of the PBL adopt the following working flow model: high Reynolds number (implying that the molecular viscosity is small and not included in the set of governing equations), incompressible, Boussinesq equations with Monin–Obukhov similarity theory as a lower boundary condition (Nieuwstadt *et al.* 1993 describe typical LES models). We mention an important difference between LES with a surface roughness ( $z_o$ ) parameterization as a lower boundary condition and LES with a resolved viscous sublayer. In the former, the SFS model contribution must be an increasingly large fraction of the total turbulence as the surface is approached whereas in the latter the SFS model becomes small near the wall with the viscous effects sufficiently large to transmit fluxes from the surface to the interior. Spalart *et al.* (1997) refers to LES with a resolved viscous sublayer as quasi-direct numerical simulation (QDNS) since the Reynolds number achievable is comparable to full DNS. Knowledge of the SFS motions over a rough wall at high Reynolds number is required to improve LES of geophysical flows.

In the LES system of equations with coordinates  $x_i = (x, y, z)$ , the total velocity  $U_i = (U, V, W)$  is formally decomposed into resolved and SFS components ( $\overline{U}_i, u_i$ ) by the application of a spatial filter  $G$  (Leonard 1974). Hence,

$$U_i = \overline{U}_i + u_i \equiv \int U_i(x'_j)G(x_i, x'_j) dx'_j + u_i. \quad (1.1)$$

The LES SFS fluxes (or stresses)  $\tau_{ij}$  are defined as

$$\tau_{ij} = \overline{U_i U_j} - \overline{U}_i \overline{U}_j \equiv L_{ij} + C_{ij} + R_{ij}, \quad (1.2)$$

where

$$L_{ij} = \overline{\overline{U}_i \overline{U}_j} - \overline{\overline{U}_i} \overline{\overline{U}_j}, \quad (1.3a)$$

$$C_{ij} = \overline{\overline{U}_i u_j} + \overline{\overline{U}_j u_i} - \overline{\overline{U}_i} \overline{u_j} - \overline{\overline{U}_j} \overline{u_i}, \quad (1.3b)$$

$$R_{ij} = \overline{u_i u_j} - \overline{u_i} \overline{u_j}. \quad (1.3c)$$

Here we adopt the Germano (1986) decomposition of the SFS flux into a modified-Leonard term $\ddagger$   $L_{ij}$ , a cross-term  $C_{ij}$ , and a SFS Reynolds stress  $R_{ij}$ . The decomposition (1.2) and (1.3) is clearly not unique but is advantageous since each term individually is Galilean invariant, independent of the type of filtering used. Alternative definitions of  $\tau_{ij}$ ,  $L_{ij}$ ,  $C_{ij}$ ,  $R_{ij}$  may or may not possess this property depending on the type of filtering applied (Speziale 1985), which then complicates the interpretation of these terms (e.g. Horiuti 1989; Härtel & Kleiser 1997). For example, based on DNS data Härtel & Kleiser (1997) found that conclusive results about SFS energy transfer can only be obtained if a Galilean-invariant form of  $L_{ij}$ ,  $C_{ij}$ ,  $R_{ij}$  is used; otherwise these terms become filter dependent.

There are few observations of  $C_{ij}$  and  $R_{ij}$  but some properties of  $L_{ij}$ , defined by (1.3a), are worth mentioning.  $L_{ij}$  depends only on resolved-scale velocities (hence no modelling is needed) and it is equivalent to the Bardina or scale-similarity term (Bardina, Ferziger & Reynolds 1983; see the review by Meneveau & Katz 2000). Also, it is the main contributor in SFS models that employ a dynamic procedure when the so-called ‘test’ filter equals the grid filter (e.g. Pope 2000, p. 622). No assumptions are used to arrive at the above formula for  $L_{ij}$ ; Bardina *et al.* (1983) arrive at (1.3a) by dropping terms in the SFS cross- and Reynolds stress tensors (1.3b), (1.3c).  $L_{ij}$  can be expanded in a Taylor series since it is smooth on the grid scale, and the expansion leads to a partial reconstruction of the total field (e.g. Winckelmans *et al.* 2001). The first term of the Taylor series expansion of  $L_{ij}$  is the basis of gradient or nonlinear SFS models (Meneveau & Katz 2000), the main component of the tensor-diffusivity model (Leonard 1997), and an important ingredient in deconvolution methods (e.g. Stolz, Adams & Kleiser 2001; Katopodes, Street & Ferziger 2000). Since  $L_{ij}$  (or a close approximation of it) can be computed directly in LES, we believe it is useful to investigate connections between  $L_{ij}$  and the cross- and Reynolds SFS stress tensors, with the expectation that this information might lead to improved SFS models.

The objective of the present study is to deduce the structure of the SFS fluxes  $\tau_{ij}$  and their component parts ( $L_{ij}$ ,  $C_{ij}$ ,  $R_{ij}$ ) from field observations in the atmospheric surface layer over a wide range of stratification. In addition, we use the measured fluxes to perform *a priori* testing of some typical SFS models currently adopted in LES. Previous work on this topic is reported by Tong *et al.* (1998) and Porté-Agel *et al.* (2001) who consider a smaller range of stratification and filter widths. Laboratory measurements reviewed by Meneveau & Katz (2000) consider lower Reynolds number and neutrally stratified flows with and without boundaries.

## 2. The field campaign

The turbulence data used here are part of the dataset collected during the Horizontal Array Turbulence Study (HATS) field program. The primary objective of HATS is the measurement of SFS variables in the surface layer of the atmospheric boundary layer using the horizontal array technique proposed by Tong *et al.* (1998) and utilized by Porté-Agel *et al.* (2001) and others. Horst *et al.* (2002) document HATS and in particular describe the field site, instrumentation and data collection procedures, assess the data quality, and evaluate the adequacy of spatial and temporal discrete filtering as a surrogate for two-dimensional spatial filtering. They conclude that the measurements of the three components of wind velocity and temperature are sufficient

$\ddagger$  We refer to  $L_{ij}$  in (1.3a) as a modified-Leonard term since it is similar in character but different from the traditional definition  $L_{ij} = \overline{U_i U_j} - \overline{U_i} \overline{U_j}$ .

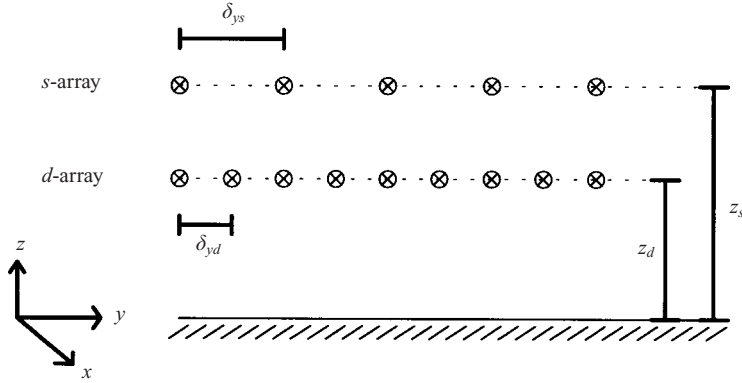


FIGURE 1. Sketch of the sonic deployment and the  $(x, y, z)$  coordinate system used for analysis. The sonic anemometers  $\otimes$  in the double and single arrays are located at  $(z_d, z_s)$  above the surface, the lateral separation between individual sonic anemometers is  $(\delta_{y_d}, \delta_{y_s})$ .

Configuration	$z_d$	$\delta_{y_d}$	$z_s$	$\delta_{y_s}$	Curve
1	3.45	3.35	6.90	6.70	●
2	4.33	2.17	8.66	4.33	$\otimes$
3a	8.66	2.17	4.33	1.08	*
3b	8.66	2.17	4.33	1.08	○
4	4.15	0.50	5.15	0.62	◇

TABLE 1. Vertical location and lateral spacing of the sonic anemometers (in m).

to accurately resolve the SFS variables and spatial  $(x, y, z)$  gradients; see Horst *et al.* (2002) for further details.

In the horizontal array technique, two arrays (or lines) of sonic anemometers are positioned perpendicular to the primary wind direction and the horizontal spacing between individual sonic anemometers is selected to achieve different spatial filter widths (see figure 1). The two sonic arrays are located at different heights above the surface to allow for measurement of vertical gradients. Under the assumption of Taylor's hypothesis in the alongwind direction, we are in essence able to measure a two-dimensional  $(x, y)$ -plane of turbulence at two levels in the atmospheric surface layer. One of the novel features of the Tong *et al.* (1998) sonic deployment is the use of a dense array of sonic anemometers to allow 'double' spatial filtering as required in (1.3). The ability to double-filter SFS variables allows us to isolate the modified-Leonard, cross- and Reynolds stress components of the SFS flux tensor (1.3).

Four different horizontal array configurations, referred to as Configuration-(1, 2, 3a, 4), are employed in HATS. Each configuration consists of a double array (or  $d$ -array) containing nine sonic anemometers and a single array (or  $s$ -array) containing five sonic anemometers. The heights  $(z_d, z_s)$  of the  $d$ - and  $s$ -arrays and lateral separation  $(\delta_{y_d}, \delta_{y_s})$  between sonic anemometers are provided in table 1. Notice that the height of the  $s$ -array is twice that of the  $d$ -array in Configuration-(1, 2), with the relative positions of the  $d$ -array and  $s$ -array reversed in Configuration-3a. (In §3 we also introduce Configuration-3b which is like Configuration-3a but with a different filter width in the  $d$ -array.) Configuration-4 is a closely packed configuration of sonic anemometers similar to that used by Porté-Agel *et al.* (2001). From these

four horizontal configurations, we can construct a wide range of filter widths (see figure 2). In the following analysis the vertical positions ( $z_d, z_s$ ) are corrected for the wind profile displacement height,  $d_o = 0.32$  m (Horst *et al.* 2002).

From the four-week database archived during HATS, a smaller subset of 35 periods (or cases) are selected for detailed analysis. All cases are at least 25 minutes in duration, are reasonably stationary in terms of wind direction and surface fluxes, and are non-overlapping (i.e. each case represents an independent period). For each configuration, the cases selected span a range of atmospheric stability varying from unstable to stable.

### 3. Analysis procedures

Resolved velocity components and temperature are generated from the measured variables in a two-stage process. First, the instantaneous horizontal (total) velocity components are transferred to new coordinates parallel and perpendicular to the mean wind direction (i.e. into alongwind and crosswind coordinates). This coordinate rotation permits us to utilize Taylor's hypothesis to convert the time-varying data at each sonic into alongwind spatial fluctuations. Next, the rotated horizontal velocity components, the vertical velocity, and temperature are interpolated to the Cartesian grid defined by alongwind and crosswind directions<sup>†</sup> (see Horst *et al.* 2002 for additional details). We utilize trigonometric (spectral) interpolation (e.g. Lanczos 1956, p. 229) in time (or equivalently in space in the alongwind direction) for this step. Spectral interpolation was found to be superior to linear interpolation, which slightly damped the high-frequency fluctuations. The average friction velocity, heat flux, and vertical velocity spectrum computed from the rotated spectrally interpolated fields are identical to their counterparts generated from the original time series.

Resolved fields are created from the rotated interpolated total fields by applying a combination of top-hat filtering in the  $y$ -direction and Gaussian filtering in the  $x$ -direction. A top-hat filter of width  $\Delta_y$  is generated from a weighted sum of five crosswind measurements. In the alongwind direction, we choose the number of data points based on mean wind speed and sample rate so that the width of the Gaussian filter  $\Delta_x = \Delta_y$ . Then the second moments of the top-hat and Gaussian filters are equal and the transfer functions of these two filters are closely matched (Horst *et al.* 2002). The two-dimensional filter width  $\Delta_f = \Delta_x = \Delta_y$ . Given our five-point top-hat filter, single-filtered (resolved) data can be generated at the middle five sonic anemometers of the  $d$ -array and at the centre sonic of the  $s$ -array (see figure 1). Time series of double-filtered data at the centre sonic of the  $d$ -array are created as needed by applying the same top-hat and Gaussian operators to single-filtered fields. The filtering software satisfies  $\overline{U_i U_j} - \overline{U_i} \overline{U_j} = L_{ij} + C_{ij} + R_{ij}$  instantaneously as required by (1.2).

In order to expand the number of available cases, we use two different width filters for the  $d$ -array of Configuration-3a. We employ a three-point top-hat filter selected to match the filter width of the  $s$ -array (we refer to this as Configuration-3a) and a wider five-point top-hat filter (Configuration-3b) constructed in the same manner as for Configurations-(1, 2, 4). Configuration-3a is well-suited for taking vertical derivatives of resolved fields since the filter widths in the  $s$ - and  $d$ -arrays are matched. On the other hand results from the  $d$ -array of Configuration-3b can be cleanly compared to

<sup>†</sup> Note that in the alongwind–crosswind grid the lateral spacing between measurement points is reduced, compared to the original sonic spacing, by the cosine of the mean wind angle.

those from Configurations-(1, 2, 4) since their filter transfer functions are identical. The difference in filter widths between the  $s$ - and  $d$ -arrays of Configuration-3b, however, lowers the accuracy of vertical derivatives.

Another aspect of the horizontal array technique is the computation of spatial gradients of resolved fields, which are required for computations of energy transfer between resolved and SFS motions (see § 5.4) and for evaluation of SFS models that utilize an eddy-viscosity prescription (see § 6). In the  $x$ - and  $y$ -directions fourth-order-accurate formulas are utilized while vertical gradients are first-order formulas based on the difference between measurements at the  $d$ -array and  $s$ -array heights (see Horst *et al.* 2002).

To quantify the statistics of total, resolved, and SFS variables, we define the temporal mean and fluctuation as

$$\alpha = \langle \alpha \rangle + \alpha' = \frac{1}{T} \int_0^T \alpha(s) ds + \alpha', \quad (3.1)$$

where  $\langle \alpha \rangle$  denotes the mean (or average) of the random variable  $\alpha$  and  $\alpha'$  is the deviation from the mean over the sample period  $T$ . The sample period is long ( $T \geq 25$  min) compared to the time scale of the filter,  $\Delta_f / \langle U \rangle$ , so that  $\langle U_i \rangle = \langle \bar{U}_i \rangle$ ,  $u'_i = u_i$ , and the decomposition of the total velocity into resolved and SFS components essentially becomes

$$U_i = \langle U_i \rangle + U'_i = \langle \bar{U}_i \rangle + \bar{U}'_i + u_i. \quad (3.2)$$

It is important to mention that while  $\langle u_i \rangle = 0$ , in general averages of higher-order moments involving  $u_i$  in the SFS flux tensor are non-zero, e.g.  $\langle \bar{u}_i \bar{u}_j \rangle \neq 0$  in the SFS Reynolds term (1.3c).

## 4. Resolved and SFS surface layer turbulence

### 4.1. Length scale

The contribution of the resolved and SFS motions to the total turbulence is determined by the position of the filter cutoff wavelength  $\Delta_f$  in the spectral distribution of turbulence energy. If the most energetic turbulent eddies are identified by the wavelength  $\Lambda$  of the spectral peak, then for cutoff and peak wavenumbers  $(k_f, k_p) = 2\pi(1/\Delta_f, 1/\Lambda)$ , the contribution of the SFS motions to the total turbulence is dominant when  $k_f \leq k_p$  while the resolved motions are of increasing importance for  $k_f \gg k_p$ . In the present investigation,  $k_f$  is set by the geometry of the experimental design (i.e. by our choice of sonic separation and filter shape) whereas  $k_p$  varies widely with the atmospheric conditions. Thus, the balance between SFS and resolved motions hinges on the sonic spacing and the state of the atmosphere. The existing body of observational evidence in the atmospheric surface layer shows that the spectral peak of the turbulent velocity and temperature fields (and their vertical flux) largely depends on the height above the surface and the atmospheric stability, as quantified by Monin–Obukhov similarity theory. A summary of surface-layer turbulence structure is given by Kaimal & Finnigan (1994). The peak wavelength of the vertical velocity,  $\Lambda_w$ , in particular varies systematically with height  $z$  and atmospheric stability as measured by the Monin–Obukhov length  $L$ ,  $z/\Lambda_w = \mathcal{H}(z/L)$ . On the other hand, the horizontal velocity components do not scale as well with Monin–Obukhov similarity because they contain large-scale motions that vary with  $z_i$ , the height of the PBL (e.g. Khana & Brasseur 1997; Johansson *et al.* 2001). In view of the importance of the vertical velocity field in the surface layer, and because  $w$  is least resolved in high-Reynolds-number LES (Peltier *et al.* 1996; Sullivan, McWilliams & Moeng

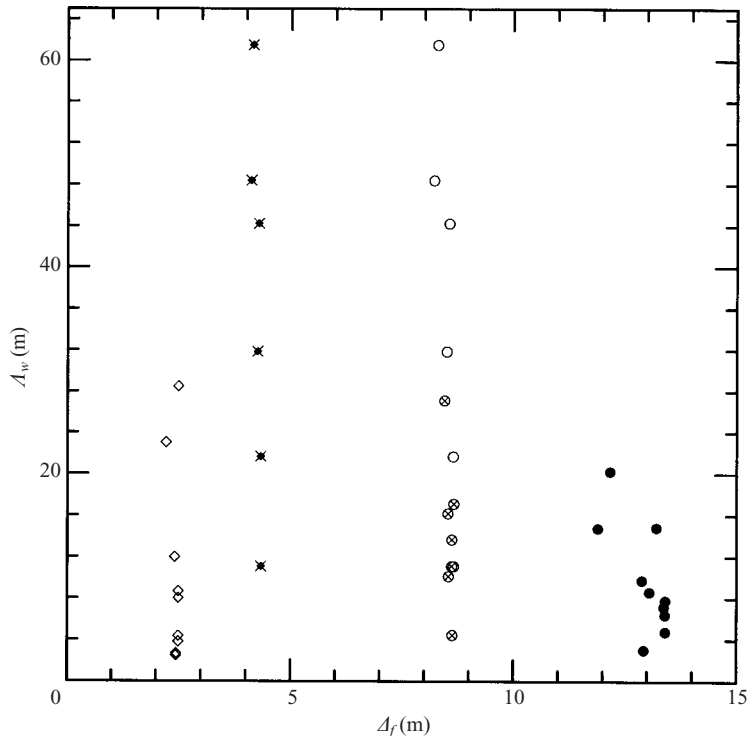


FIGURE 2. The  $(\Lambda_w, \Delta_f)$  parameter space for the observational campaign.  $\Lambda_w$  is the wavelength of the peak energy in the vertical velocity and  $\Delta_f$  is the filter width. The particular configurations of sonic anemometers (see table 1) are denoted by the symbols ( $\bullet$ ,  $\otimes$ ,  $*$ ,  $\circ$ ,  $\diamond$ ) and are used in all following figures.

1996), we adopt the peak wavelength of the vertical velocity field  $\Lambda_w$  as the relevant surface-layer turbulence length scale in the subsequent analysis. Other choices for a length scale may also be useful in the analysis of SFS turbulence. For example, Meneveau & Lund (1997) use the Kolmogorov microscale  $\eta = (\nu^3/\epsilon)^{1/4}$  ( $\nu$  is the molecular viscosity and  $\epsilon$  the viscous dissipation rate) because their filter cutoff scale is near the viscous dissipation scale. Porté-Agel *et al.* (2001) use the height  $z$  above the surface in their analysis of SFS heat flux for a limited range of atmospheric stability,  $-0.35 < z/L < -0.15$ .

We utilize two assumptions to obtain estimates of  $\Lambda_w$ : Taylor's hypothesis and an analytic form for the one-dimensional  $w$ -spectrum based on the exponential autocorrelation function  $R(t) = \exp(-t/\tau_p)$  (Kaimal & Finnigan 1994, p. 63). Under these assumptions,  $\Lambda_w = 2\pi\langle U \rangle \tau_p$  where  $\langle U \rangle$  is the mean velocity in the alongwind direction and  $\tau_p$  is the Eulerian integral time scale. In practice, we compute the autocorrelation function of the vertical velocity and linearly interpolate in time to find the location that yields  $R(\tau_p = t) = e^{-1}$ . The results are well behaved and avoid ambiguities associated with finding a peak by a fitting procedure applied to the spectrum. The exponential autocorrelation function implies a large-wavenumber spectrum  $\sim k^{-2}$ , but we find only small differences (10%–15%) in  $\Lambda_w$  for analytic functions that predict a large-wavenumber spectrum  $\sim k^{-5/3}$  (Horst *et al.* 2002).

The  $(\Lambda_w, \Delta_f)$  parameter space for the field campaign is illustrated in figure 2.  $\Delta_f$  changes by more than a factor of 5 for narrow and wide sonic spacings, while varying

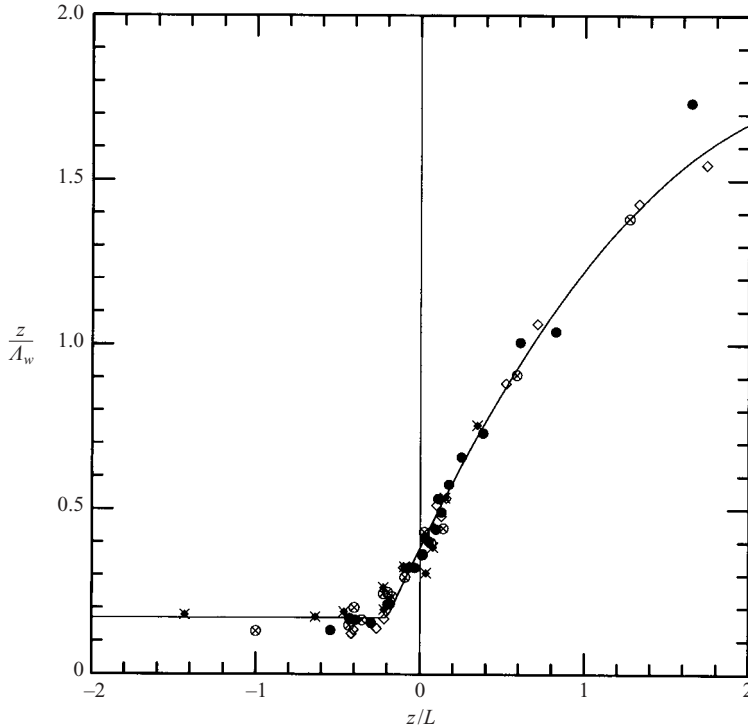


FIGURE 3. Variation of the wavelength of the vertical velocity spectral peak  $\Lambda_w$  with atmospheric stability  $z/L$ . Results for both  $d$ - and  $s$ -arrays are included. The solid line is a curve fit to the data given by (4.5).

atmospheric conditions and sonic height cause  $\Lambda_w$  to change by a factor of 10 or more. The slight changes in  $\Delta_f$  for a given array of sonic anemometers are induced by variations in the horizontal wind direction (i.e. the mean wind is not always perpendicular to the line of sonic anemometers). Cases with mean winds mis-aligned (relative to the line of sonic anemometers) always lead to smaller filter widths (see §3). The dependence on vertical height is also observed in figure 2 where  $\Lambda_w$  is largest for Configuration-(3a,3b), i.e. the sonic configuration located at the greatest height. Note that the filter widths of Configuration-(3a,3b) are different as discussed in §3. The ratio  $\Lambda_w/\Delta_f$  (which we refer to as the energy-filter ratio) spans the interval  $[0.2, 15]$  (a factor of about 75) and thus the balance between SFS and resolved motions also varies widely (see §5). The SFS motions are dominated by large turbulent eddies, relative to the filter scale, when  $\Lambda_w/\Delta_f < 1$  and by small-scale turbulent eddies when  $\Lambda_w/\Delta_f \gg 1$ .

Figure 3 shows the variation of  $z/\Lambda_w$  with stability for the cases considered, along with a curve fit to the data (see §4.2). As no aspects of filtering are involved in computing  $\Lambda_w$ , we show the average of all measurements at a fixed height. Thus, for a particular horizontal array configuration we obtain two estimates: an average of 9 sonic anemometers in the  $d$ -array and 5 sonic anemometers in the  $s$ -array. The results collapse well to a single curve for the wide range of stabilities and vertical locations considered. For a fixed  $z$ , the spectral peak of the vertical velocity dramatically shifts towards higher wavenumbers with increasing stability, and thus  $z/\Lambda_w$  changes by more than a factor of 10 for the range  $-1 < z/L < 1$ . Our measurements are

generally consistent with results previously reported by Kaimal *et al.* (1972, 1976, 1982) and Panofsky & Dutton (1984) for the atmospheric surface layer over a rough surface with no large-scale inhomogeneity. The impact of the  $\Lambda_w$  dependence on stability for LES is discussed below.

#### 4.2. Surface-layer LES

Past experience suggests that surface-layer turbulence is poorly resolved in LES, more so with increasing atmospheric stability. To quantify this perception we need to relate measurements of SFS quantities to LES, and in particular determine the values of  $\Lambda_w/\Delta_f$  for typical LES grid spacings and shear–buoyancy forcing. Surprisingly, the LES filter width is not well defined in most implementations and a clean comparison between  $\Delta_f$ -LES and  $\Delta_f$ -observations cannot be made. The SFS model for typical LES is posed in terms of resolved (filtered) fields and explicit spatial filtering is not formally required to solve the system of equations, i.e. only  $\overline{U}_i$  appears in the momentum equations of an LES. Spatial filtering is performed implicitly with the SFS model and the differencing scheme. For instance, the Smagorinsky SFS model imposes a filter similar in shape to a Gaussian filter at high wavenumbers (Pope 2000, p. 590; see also Mason & Callen 1986; Mason & Brown 1999). Furthermore, finite-difference and finite-volume codes employ low-order difference operators on anisotropic grids, and as a result the SFS model physics is mixed with the numerical errors (Ghosal & Moin 1995; Scotti, Meneveau & Fatica 1997). Boundary layers pose an added complication since the presence of a solid wall invalidates the assumption of spatially homogeneous filtering and then the filter width is dependent on the distance from the boundary. Explicit spatial filtering, which is computationally expensive, is employed with pseudospectral LES codes (e.g. Rogallo & Moin 1984; Bardina *et al.* 1983; Moeng & Wyngaard 1988) to control aliasing errors and also with LES models that employ SFS models based on multiple filterings of the resolved field (e.g. Winckelmans *et al.* 2001). The latter LES implementations utilize a more precise definition of filter width.

To illustrate the connection between observations and LES and to establish a basis for the interpretation of our measurements, we adopt the definition of filter width in our mixed finite-difference pseudospectral code (Moeng & Wyngaard 1988; Sullivan *et al.* 1996). In this code, the LES filter width is based on the cell volume

$$\Delta_{f,les}^3 = c_1^2 \delta x \delta y \delta z, \quad (4.1)$$

where  $(\delta x, \delta y, \delta z)$  are grid spacings and the constant  $c_1 = 3/2$ . Computed fields are explicitly filtered in the  $x$ - and  $y$ -directions at the filter cutoff scales  $(\Delta_x, \Delta_y) = c_1(\delta x, \delta y)$ . A similar definition of  $\Delta_{f,les}$  was first proposed by Deardorff (1970) and is employed in finite-difference LES codes that utilize explicit filtering on anisotropic grids (e.g. Katopodes *et al.* 2000). In the absence of boundaries, the use of the cell volume to define the filter width is formally justified by Scotti, Meneveau & Lilly (1993). For simplicity, we set  $\delta y = \delta x$  (which is frequently used) and then the expression for the LES filter width (4.1) becomes

$$\Delta_{f,les} = \delta z (R_c c_1)^{2/3}, \quad (4.2)$$

which depends on only two parameters:  $\delta z$ , and the mesh aspect ratio  $R_c = \delta x/\delta z$ . The variation of the spectral peak of the vertical velocity with atmospheric stability is reasonably well established from the observational results given in figure 3. Hence,

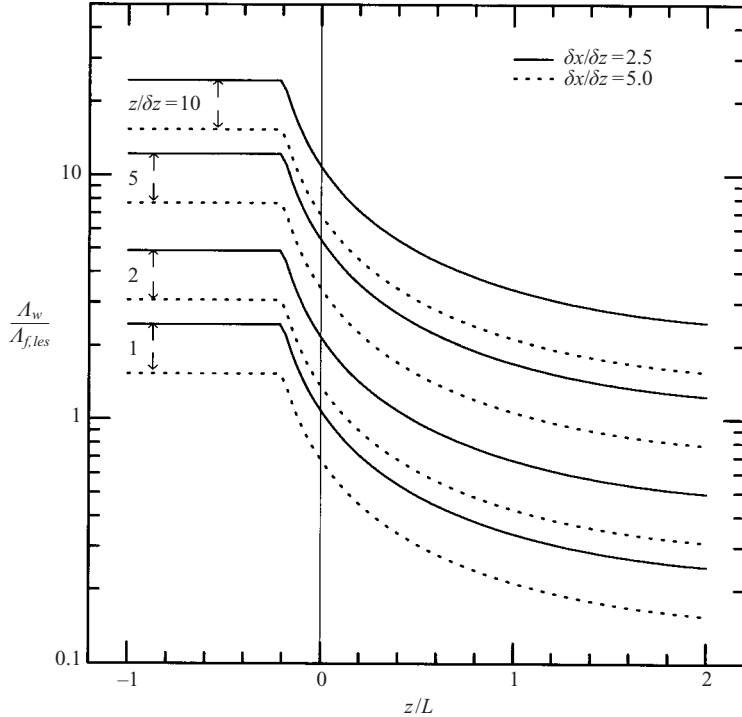


FIGURE 4. Ratio of the peak vertical velocity scale  $\Lambda_w$  to the LES filter width  $\Delta_{f,les}$  for the atmospheric surface layer. For a particular height above the surface  $z/\delta z$  the family of curves shows the variation with the mesh aspect ratio  $R_c = \delta x/\delta z$ .

we assume the functional form

$$\Lambda_w = z/\mathcal{H}(z/L), \quad (4.3)$$

which combined with (4.2) leads to

$$\frac{\Lambda_w}{\Delta_{f,les}} = \frac{z}{\delta z} \frac{(R_c c_1)^{-2/3}}{\mathcal{H}(z/L)}. \quad (4.4)$$

The variation of  $\Lambda_w/\Delta_{f,les}$  given by (4.4) is shown in figure 4 with  $\mathcal{H}(z/L)$  determined from a least-squares curve fit to the data in figure 3. The functional form is

$$\mathcal{H}(z/L) = \begin{cases} 0.17, & z/L \leq -0.2 \\ 0.38 + z/L(1.04 - 0.2z/L), & -0.2 < z/L < 2. \end{cases} \quad (4.5)$$

In figure 4,  $z/\delta z = 10$  corresponds to the upper boundary of the surface layer  $z_{sl} \approx 0.1z_i$  for a simulation with  $N_z = 200$  equally spaced vertical nodes with half of the nodes located between the surface and the top of the mixed layer ( $z_i = N_z \delta z/2$ ). Note that coarser (finer) vertical resolution pushes the top of the surface layer towards smaller (larger) values of  $z/\delta z$ . Mesh aspect ratios  $R_c = (2.5, 5.0)$  are representative of LES; a value of 2.5 is often used in our simulations of the atmospheric PBL (e.g. Moeng & Wyngaard 1988; Moeng & Sullivan 1994; Dubrulle *et al.* 2002).

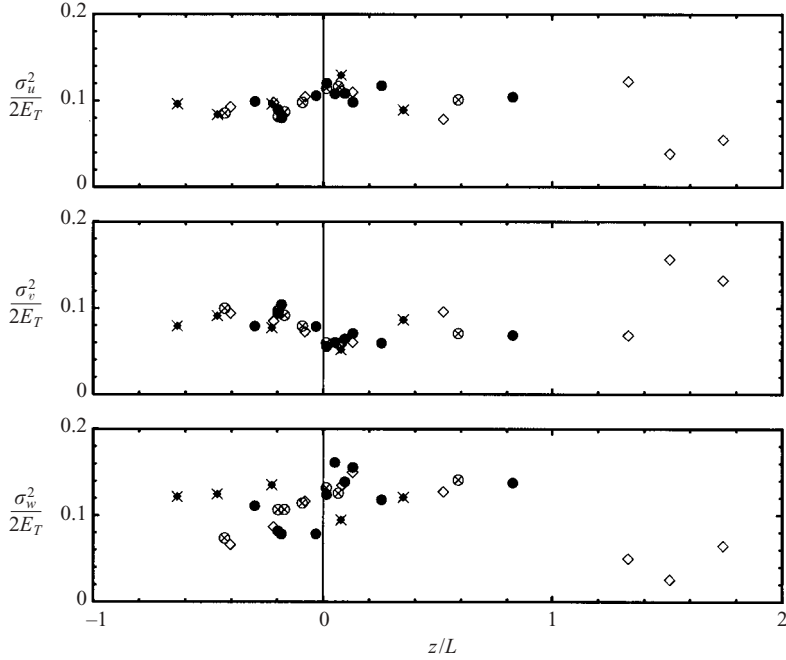


FIGURE 5. Variances of the total turbulence ( $\sigma_u^2$ ,  $\sigma_v^2$ ,  $\sigma_w^2$ ) normalized by the total turbulence kinetic energy  $E_T$  for varying atmospheric stabilities.

The energy-filter ratio  $\Lambda_w/\Delta_{f,les}$  is observed to be a strongly decreasing function with increasing stability ( $z/L$ ) in the surface layer. This is a direct consequence of the behaviour of the wavelength of the spectral peak ( $\Lambda_w$ ) in figure 3. For all combinations of  $z/\delta z$  and mesh aspect ratios considered,  $\Lambda_w/\Delta_{f,les}$  (or  $k_f/k_p$ ) attains its maximum value under unstable conditions  $z/L < -0.2$ . At the first grid point above the surface  $z/\delta z = 1$  and  $R_c = 2.5$ , the ratio  $\Lambda_w/\Delta_{f,les}$  reaches a maximum of about 2.5 for unstable conditions, falls to 1.0 for neutral conditions, and is less than 0.5 for a stability of  $z/L = 0.5$ . Note that increased vertical grid resolution drives  $z/L \rightarrow 0$  (neutral) but does not alter the variation in figure 4. If  $\delta z$  is reduced, accompanied by consistent changes in  $\delta x$ , then the same variation occurs but closer to the wall. At neutral stability  $\mathcal{H}(0)$  is independent of  $z$  and at the first grid point (4.4) reduces to a constant. In other words, both  $\Lambda_w$  and  $\Delta_{f,les} \sim z$  (see also Juneja & Brasseur 1999). The energy-filter ratio of interest for LES in the surface layer, encompassing a wide spectrum of buoyancy–shear forcing, ranges from about  $0.1 < \Lambda_w/\Delta_{f,les} < 20$  and for the majority of atmospheric conditions, the vertical velocity spectrum at  $k_f$  is not proportional to  $k_f^{-5/3}$  as expected in the inertial subrange.

In the following analysis, results are presented as functions of the energy filter ratio  $\Lambda_w/\Delta_f$  since it contains the essential information about stratification, height, and filter width. Thus, all measured SFS statistics collapse reasonably well in terms of this parameter. Furthermore, the ratio  $\Lambda_w/\Delta_f$  allows us to connect measurements of SFS variables with LES applications.

#### 4.3. Energy distribution

Much of the analysis and interpretation of the SFS motions (described in § 5) is closely linked to the total turbulent kinetic energy (TKE) and its partitioning amongst the velocity components. In figure 5, the energy distribution in the ( $u$ ,  $v$ ,  $w$ ) components

with varying atmospheric stability ( $z/L$ ) is displayed. The average velocity variance of the total turbulence is

$$\sigma_i^2 = \langle [U_i - \langle U_i \rangle]^2 \rangle, \quad (4.6)$$

and thus the average TKE,  $E_T = (\sigma_u^2 + \sigma_v^2 + \sigma_w^2)/2$ . As expected in the surface layer, the  $u$ - and  $v$ -variances are dominant, with their sum accounting for approximately 80% to 85% of the total energy. Closer inspection of the data hints that  $\sigma_u^2 > \sigma_v^2$ , especially near neutral stability, a likely consequence of production by mean wind shear  $\partial \langle U \rangle / \partial z$ . The proximity of the surface inhibits vertical motions and as a result the  $w$ -variance is about a factor of 2 to 3 smaller than the horizontal variances. This partitioning of normalized energy amongst the velocity components is nearly uniform across the range of stabilities considered.

## 5. Attributes of observed SFS motions

### 5.1. Energy, variances, and vertical momentum

The contribution of the SFS motions to the total turbulence energy, variances, and vertical momentum flux is depicted in figure 6 for varying energy-filter ratio  $\Lambda_w/\Delta_f$ . Here the SFS energy  $E_s = \tau_{ii}/2$ , variances, and momentum flux are generated from the (instantaneous) total and resolved velocity fields ( $U_i, \bar{U}_i$ ) using (1.2). Because (1.2) is a flux conservation rule, i.e. total flux equals resolved plus SFS fluxes, we can also infer the resolved contributions from figure 6. For example, the normalized resolved  $u$ -variance is  $1 - \langle \tau_{11} \rangle / \sigma_u^2$ . Figure 6 clearly illustrates the following. First, the shifting balance between resolved and SFS energy and variances depends on the location of the filter scale relative to the spectral peak of the turbulence. At  $\Lambda_w/\Delta_f = 1$ , for example, the balance between resolved and SFS energy is  $\approx 50\%$  while the SFS contribution decreases to  $\approx 15\%$  for  $\Lambda_w/\Delta_f \geq 10$ . Second, the results collapse reasonably well in terms of the ratio  $\Lambda_w/\Delta_f$  over a wide range of stabilities and filter widths as evidenced by the overlap for the different array configurations. The collapse of the SFS  $w$ -variance for different filter widths and atmospheric conditions is especially good, and provides further evidence that  $\Lambda_w$  closely tracks the scale of the energy-containing eddies in the vertical velocity spectrum. SFS ( $u, v$ )-variances exhibit more scatter, especially for small values of  $\Lambda_w/\Delta_f$  with stable conditions. In this situation,  $u_i \approx U_i$  and the horizontal SFS motions contain larger-scale meandering eddies which are not described by surface-layer scaling (e.g. Kaimal & Finnigan 1994; Khana & Brasseur 1997). Notice that for any particular value of energy-filter ratio  $\langle \tau_{33} \rangle / \sigma_w^2 > \langle \tau_{11} \rangle / \sigma_u^2$  and  $\langle \tau_{22} \rangle / \sigma_v^2$ . This is a consequence of the spectral distribution of the total velocity fields, where  $w$  is shifted to higher wavenumbers compared to ( $u, v$ ). This same spectral distribution holds for the SFS velocities and thus the normalized SFS vertical velocity variance is largest.

The SFS vertical momentum flux  $\langle \tau_{13} \rangle$  (see figure 6) is of prime concern in LES as it is a pathway for momentum exchange between the surface layer and the mixed layer in the PBL. The variation of  $\langle \tau_{13} \rangle$  is comparable to the SFS  $w$ -variance and its contribution to the total vertical momentum flux is significant – at least 50% for  $\Lambda_w/\Delta_f \leq 2$ . Our measurements of SFS energy, variances, and fluxes support our proposal to use  $\Lambda_w/\Delta_f$  as a scaling parameter and emphasize the dependence of the SFS motions on both  $z$  and  $L$  in the surface layer. Plotting the SFS energy, variances, and fluxes as a function of the ratio  $z/\Delta_f$  would introduce large scatter for any particular array configuration and a typical diurnal range of stability.

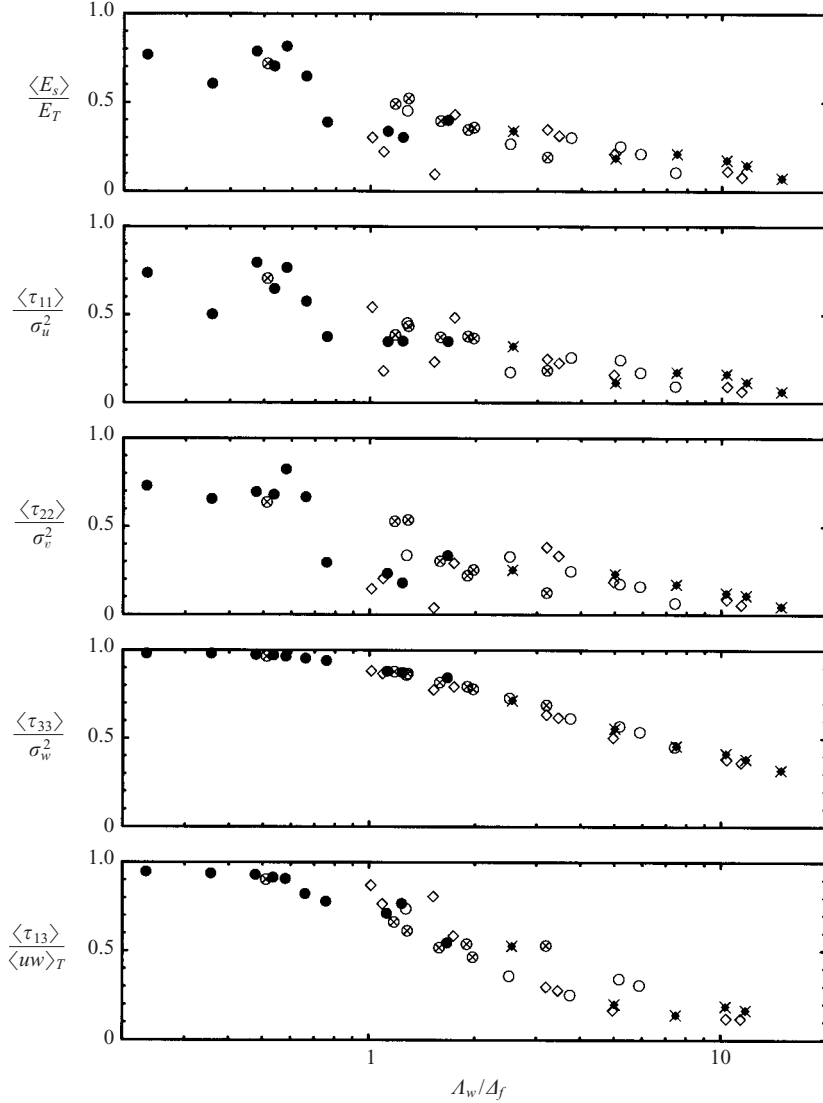


FIGURE 6. Fraction of energy, variances, and vertical momentum flux contained in the SFS motions for varying energy-filter ratio  $\Lambda_w/\Delta_f$ .  $\langle E_s \rangle$ ,  $\langle \tau_{ii} \rangle$ ,  $\langle \tau_{13} \rangle$  are normalized by their respective total counterparts.

### 5.2. Anisotropy

Classical SFS models for LES that utilize a Smagorinsky or TKE formulation (see §6), assume a Kolmogorov inertial-range spectrum and isotropy at the filter scale. The validity of the latter assumption for SFS motions in a stratified surface layer is, however, unknown. A test of isotropy for SFS variables is presented in figure 7 where we show the measures  $3\langle \tau_{11}, \tau_{22}, \tau_{33} \rangle / 2\langle E_s \rangle$  with varying energy-filter ratio. These ratios are unity for strict adherence to isotropy. The isotropy measures for the  $(\tau_{11}, \tau_{22}, \tau_{33})$  components are  $(> 1, \approx 1, < 1)$ , respectively, and exhibit small scatter for all  $\Lambda_w/\Delta_f$ . The  $\tau_{11}$  and  $\tau_{33}$  components are anisotropic because of a prevailing mean

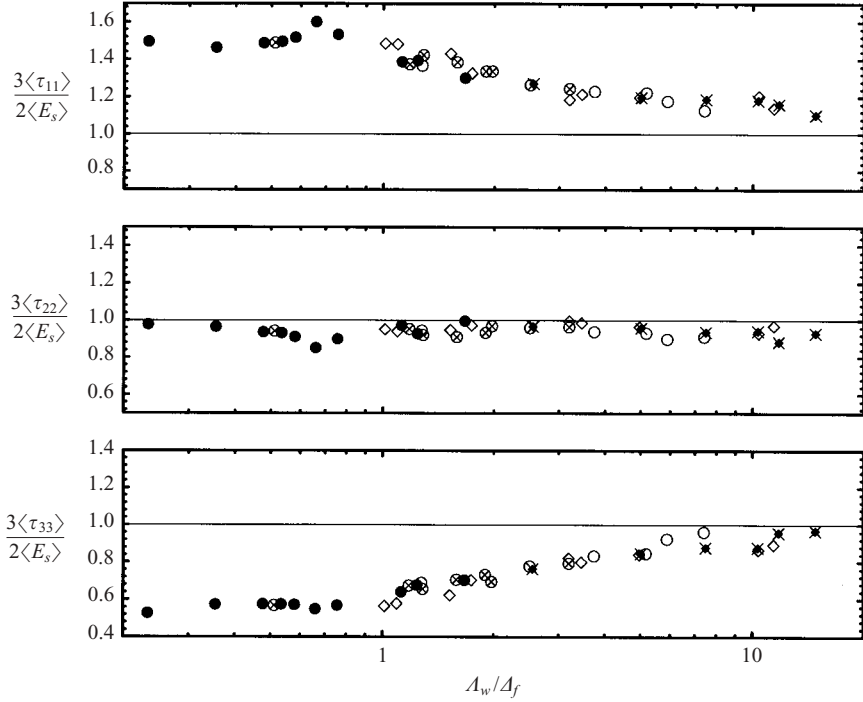


FIGURE 7. SFS variances normalized by the SFS energy for varying  $\Lambda_w/\Delta_f$ . The SFS variances are isotropic when  $3\tau_{ii}/2E_s = 1$ .

wind and the proximity of the surface. These results indicate that the SFS variances approach isotropy only for quite large values of the energy-filter ratio,  $\Lambda_w/\Delta_f > 10$ .

Properties of the total deviatoric Reynolds-stress tensor are used in second-order closure modelling (Pope 2000) and also in conjunction with DNS databases of channel flow (e.g. Antonia & Kim 1994) to quantify turbulence anisotropy. We adopt a similar measure and assess the anisotropy of the SFS fluxes in the atmospheric surface layer by investigating the properties of the normalized anisotropic SFS tensor

$$b_{ij} = \frac{\langle \tau_{ij} \rangle}{\langle \tau_{kk} \rangle} - \frac{1}{3}\delta_{ij}, \quad (5.1)$$

where  $\delta_{ij}$  is the Kronecker delta and again  $\langle \cdot \rangle$  denotes a temporal average. In a realizable turbulent flow  $b_{ij}$  is a real symmetric matrix with three real eigenvalues  $\lambda_i$  that define principal axes (i.e. in principal axes  $b_{ij}$  has only diagonal elements). (Principal axes decomposition has been used extensively to examine the orientation of stress and strain in turbulent flows (e.g. Tao, Katz & Meneveau 2000).) Three matrix invariants can be constructed from linear combinations of  $\lambda_i$  and these invariants uniquely describe the anisotropy of the SFS stress, instead of the original six components of  $b_{ij}$ . Since  $b_{ij}$  is deviatoric, i.e. traceless with  $\lambda_1 + \lambda_2 + \lambda_3 = 0$ , only two of the invariants are unique and are sufficient to fully describe  $b_{ij}$ . We follow Pope (2000, p. 393) and define the invariants  $(\xi, \eta)$  of the SFS anisotropy tensor as

$$6\xi^3 = 3(\lambda_1\lambda_2\lambda_3), \quad (5.2a)$$

$$6\eta^2 = -2(\lambda_1\lambda_2 + \lambda_2\lambda_3 + \lambda_1\lambda_3). \quad (5.2b)$$

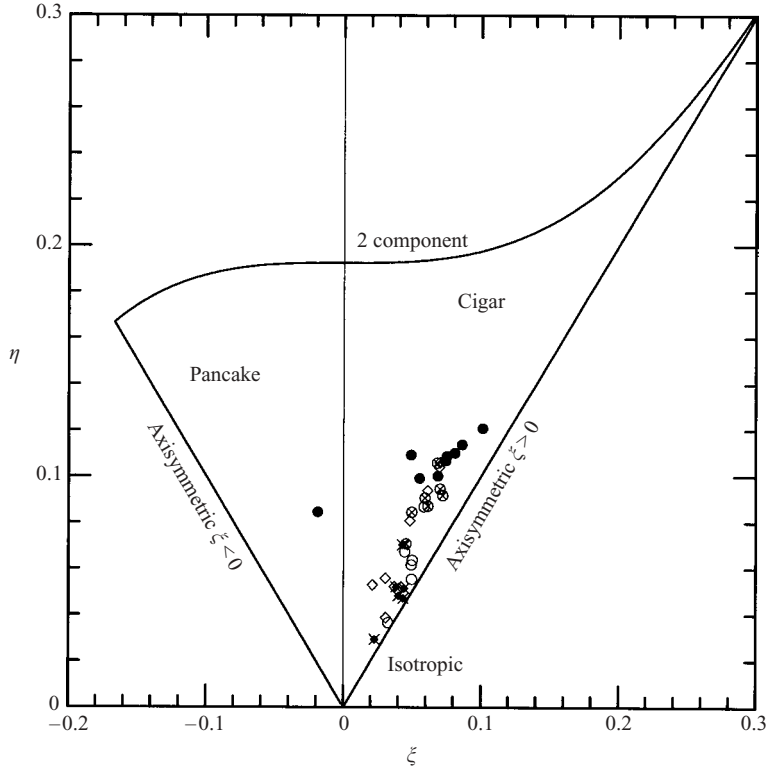


FIGURE 8. Lumley invariants of the average deviatoric SFS stress tensor for all cases. The boundaries of the Lumley triangle (Pope 2000), denoted by solid lines, correspond to special turbulence states.

The invariants  $(\xi, \eta)$ , computed from the eigenvalues of the measured SFS stress, are presented in figure 8 for varying  $\Lambda_w/\Delta_f$ . In a turbulent flow all combinations of the invariants  $(\xi, \eta)$  must fall within the boundaries of the Lumley triangle (Lumley 1978, see also Pope 2000). These boundaries, denoted by solid lines in figure 8, correspond to special states of the turbulent flow as labelled in the figure. Our measurements indicate that the preferred (average) state of the deviatoric SFS flux tensor is closest to axisymmetric, but with a strong dependence on the atmospheric conditions and filter width. The lower range of the data points (smaller  $\xi, \eta$  values) tends towards isotropy and closely follows the variation of the energy-filter ratio; the lower range corresponds to unstable atmospheric conditions with a filter cutoff wavenumber far to the right of the spectral peak ( $\Lambda_w/\Delta_f \gg 1$ ) and hence to SFS fluxes nearest the isotropic state. This agrees with the earlier observations of the SFS variances (see figure 7).

In the right half of the Lumley triangle, the shape of the SFS tensor is classified as a prolate spheroid (Pope 2000, p. 394), i.e. the SFS tensor is a ‘cigar’ shape. Average values of the Reynolds-stress tensor, obtained from DNS of neutral low- $Re$  channel flows, also exhibit a similar bias towards axisymmetric ( $\xi > 0$ ) turbulence especially in the near wall region but outside the viscous sublayer (see Pope 2000, figure 11.1). One of our measurements, however, clearly falls in the regime indicative of a ‘pancake’ shaped SFS flux tensor. In this particular case, the atmosphere is strongly stable ( $z/L = 1.7$ ) and approximately 40% of the turbulent energy is SFS;

$\Lambda_w/\Delta_f = 1.7$ . Pancake shaped eddies are frequently associated with stably stratified flows; the presence of stable vertical stratification inhibits vertical motions, resulting in anisotropic turbulence (e.g. Kimura & Herring 1996; Riley & LeLong 2000). Our isotropy analysis of the SFS motions also supports the traditional view of turbulence that the large-scale turbulent eddies contain most of the anisotropy. Recall that as  $\Lambda_w/\Delta_f$  decreases, the SFS motions are increasingly dominated by large scales.

The degree of anisotropy in the SFS tensor and energy components has important implications for LES. Our results suggest that the turbulence fields must be very well resolved in the surface layer to satisfy the isotropy assumption under which the majority of SFS models are built (i.e.  $\Lambda_w/\Delta_f > 10$ ). In this regard, it is important to mention that the two-dimensional filtering used here is isotropic; the  $x$  and  $y$  filter widths are matched. Thus the filtering does not bias the SFS turbulence towards an anisotropic state; Kaltenbach (1997) notes that anisotropic filters can provide false information about isotropy in LES calculations.

### 5.3. Modified-Leonard, cross-, and Reynolds terms

Further decomposition of the SFS tensor into modified-Leonard, cross-, and Reynolds terms is desirable to gain insight into the interconnections between resolved and SFS motions and also to provide guidance for specific SFS modelling assumptions. The choice of filter and SFS decomposition, however, add to the confusion about the properties of these three tensors. As noted earlier, we adopt the Germano decomposition of the SFS tensor (see equations (1.2) and (1.3)) primarily based on its Galilean invariant properties, which hold irrespective of the filter type. Hence, the relative contribution of  $L_{ij}$ ,  $C_{ij}$  and  $R_{ij}$  to the particular SFS flux of interest can be assessed without contamination by the mean flow. Compared to  $\tau_{ij}$ , computation of  $L_{ij}$ ,  $C_{ij}$  or  $R_{ij}$  is more complex requiring double filtering of the velocity fields. (An example is  $L_{11} = \overline{\overline{U}} \overline{\overline{U}} - \overline{\overline{U}} \overline{\overline{U}}$ .) We apply the filtering operations as described in §3 to estimate the various components of the  $L_{ij}$ ,  $C_{ij}$ , and  $R_{ij}$  flux tensors according to their definitions (1.3).

The decomposition of the SFS normal stresses and  $uw$ -vertical flux component (displayed in figure 6) into modified-Leonard, cross-, and Reynolds terms is shown in figures 9, 10, 11 and 12, respectively; no results are presented for the smaller  $\tau_{12}$  and  $\tau_{23}$  components. First, the mean values of all tensor components vary smoothly with the energy-filter ratio and are of comparable magnitude. This contrasts with Galilean variant definitions of  $L_{ij}$  and  $C_{ij}$  that lead to large Leonard terms and cross-terms of nearly opposite sign (e.g. Horiuti 1989; Härtel & Kleiser 1997). The SFS Reynolds term is dominant at small  $\Lambda_w/\Delta_f$ , where it can account for more than 90% of the SFS tensor, whereas at large  $\Lambda_w/\Delta_f$  the partitioning amongst the modified-Leonard, cross-, and Reynolds normal stresses is about (25, 20, 55)%, respectively. The variation at  $\Lambda_w/\Delta_f \ll 1$  tends to an asymptote. For very large filter widths the turbulent fluxes must be entirely SFS,  $\tau_{ij} \rightarrow R_{ij}$  and  $R_{ij}$  tends to the ensemble-average Reynolds stress.

In the range  $\Lambda_w/\Delta_f$  greater than about 2, the resolved motions are of increasing importance compared to their SFS counterparts as the filter cutoff wavenumber begins to encroach into the inertial range of the turbulence. The observations show that the diagonal components  $L_{ii}$  and  $C_{ii}$  each contribute about 20% to 25% to the SFS variances (i.e.  $R_{ii}$  decreases to about 50%–60% of the SFS variance) when  $\Lambda_w/\Delta_f > 2$ . Because the spectral peak of  $w$  is shifted to higher wavenumbers compared to  $u$  and  $v$ , the normalized  $R_{33}$  is larger than the normalized ( $R_{11}$ ,  $R_{22}$ ). This is most apparent at small  $\Lambda_w/\Delta_f$ . Meanwhile a different balance is observed in

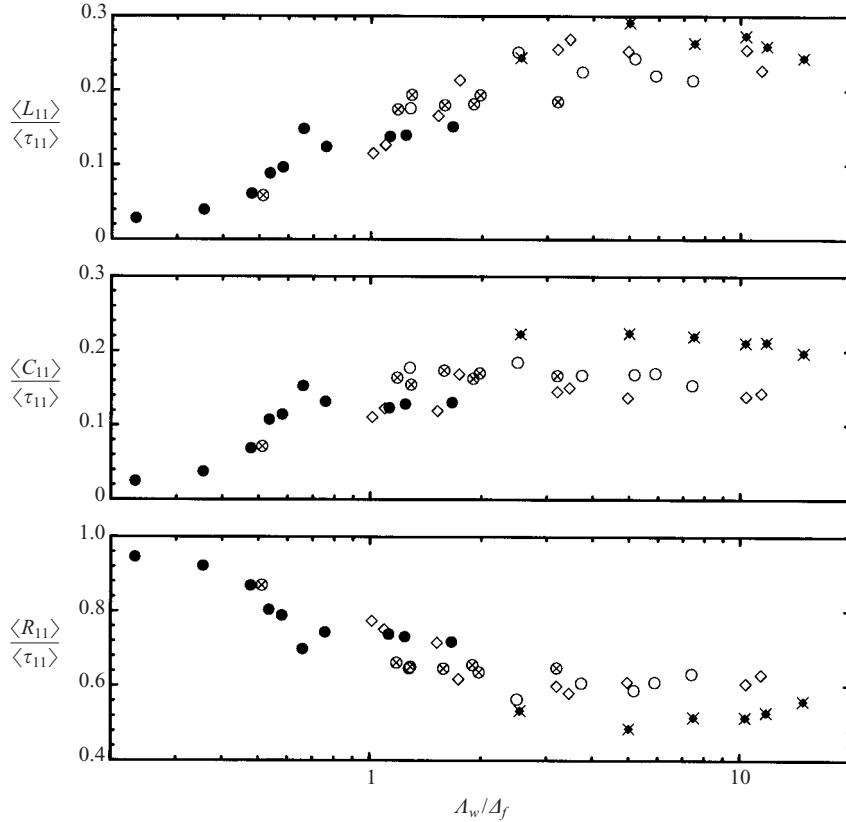


FIGURE 9. Decomposition of  $\tau_{11}$  flux into modified-Leonard, cross-, and Reynolds terms for varying atmospheric stability and filter width.

the SFS vertical momentum. Although  $R_{13}$  is dominant at small  $\Lambda_w/\Delta_f$ ,  $L_{13} > R_{13}$  and  $C_{13} \approx R_{13}$  for energy-filter ratios  $>3$ ; proportionally ( $L_{13}, C_{13}$ ) can be as much as (50, 30)% of the vertical momentum flux. Tong, Wyngaard & Brasseur (1999) also reported that cross-terms were large for the SFS vertical momentum flux. A rigorous comparison with Tong *et al.* (1999), however, is difficult since they used a combination of spectral and top-hat filtering (presumably no Leonard term) and a different definition of the SFS tensor.

The large contribution of the modified-Leonard term to the total SFS tensor is noteworthy. For filter functions that are positive in physical space (e.g. top-hat and Gaussian filters),  $L_{ij}$  is a critical term as it contributes to the SFS flux and energy transfer (see §5.4) and potentially provides clues for SFS models (see §6.2). In physical space,  $L_{ij}$  contains information about nonlinear interactions between resolved scales, some of which cascade energy to smaller scales slightly above and below the filter cutoff scale. The scale content of fluctuating  $L_{ij}$  is comparable to the other SFS stress components over a wide range of  $\Lambda_w/\Delta_f$  as illustrated in figure 13 for the (1,3)-component. At small  $\Lambda_w/\Delta_f$  ( $=0.58$ ; figure 13a), the  $L_{ij}$  fluctuations are about one order of magnitude smaller than the cross-term and two orders of magnitude smaller than the Reynolds term. As the filter cutoff moves towards higher wavenumbers ( $\Lambda_w/\Delta_f = 11.4$ ; figure 13b), this partitioning shifts such that the fluctuations in  $L_{ij}$  are of comparable magnitude to  $C_{ij}$  and  $R_{ij}$  at all wavenumbers. This behaviour of

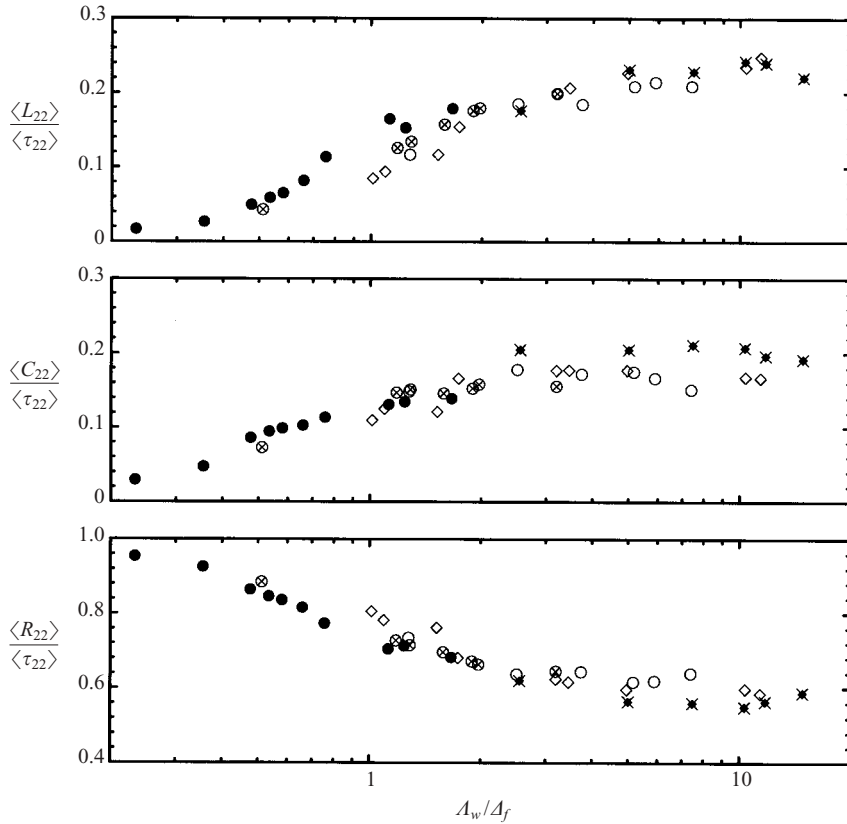


FIGURE 10. Decomposition of  $\tau_{22}$  flux into modified-Leonard, cross-, and Reynolds terms.

$L_{ij}$  helps explain the good performance of mixed SFS models as  $\Lambda_w/\Delta_f$  varies from values less than unity to values greater than unity (see § 6.2).

#### 5.4. Energy transfer

Energy exchange between large- and small-scale motions is a critical process in turbulent flows and plays an important role in the development and analysis of SFS models. For example, in the inertial range of turbulence the assumption that production of small-scale turbulence is approximately equal to dissipation leads to the classical Smagorinsky and TKE models and provides a theoretical basis for computing model coefficients (e.g. Lilly 1967; Moeng & Wyngaard 1988). Although the net energy exchange is such that small scales act dissipatively on large scales, the instantaneous flow of energy between small and large scales can be of either sign, i.e. from large to small scales (forwardscatter) or from small to large scales (backscatter). DNS databases have been used extensively to investigate the directional exchange of energy (e.g. Piomelli *et al.* 1991; Piomelli, Yu & Adrian 1996), and theoretical models have been proposed for incorporating the backscatter process in the equations for the resolved scales (e.g. Leith 1990; Mason & Thomson 1992; Schumann 1995). Mason & Thomson (1992) include a stochastic backscatter model in their atmospheric LES and maintain that the inclusion of backscatter is an important correction to LES modelling of surface layer turbulence in neutral conditions.

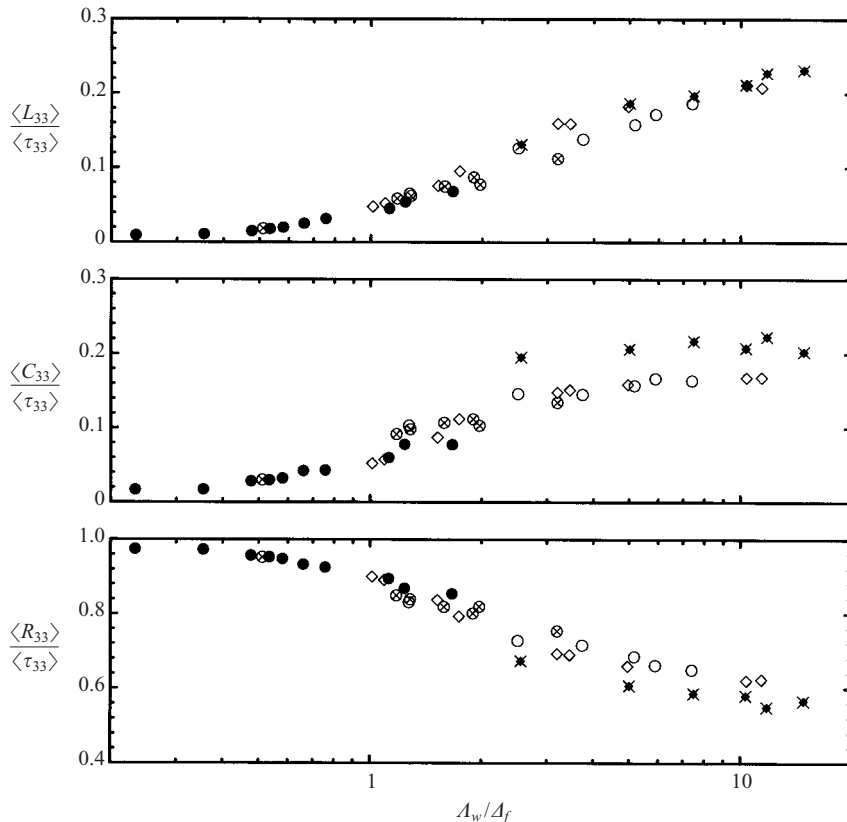


FIGURE 11. Decomposition of  $\tau_{33}$  flux into modified-Leonard, cross-, and Reynolds terms.

The present dataset provides an opportunity to investigate the energy exchange between resolved and SFS motions at high Reynolds number and assess the importance of backscatter. Production of SFS energy by the resolved scales is

$$\mathcal{P} = -\tau_{ij} S_{ij}, \quad (5.3)$$

where the resolved-scale strain rate tensor is

$$S_{ij} = \frac{1}{2} \left( \frac{\partial \bar{U}_i}{\partial x_j} + \frac{\partial \bar{U}_j}{\partial x_i} \right). \quad (5.4)$$

With our sign convention, positive (negative) production of SFS energy  $\mathcal{P}$  is forwardscatter (backscatter). The forwardscatter and backscatter components of the SFS energy production (Piomelli *et al.* 1991)

$$\mathcal{P}_f = \frac{1}{2}(\mathcal{P} + |\mathcal{P}|), \quad \mathcal{P}_b = \frac{1}{2}(\mathcal{P} - |\mathcal{P}|), \quad (5.5)$$

are computed using the measured SFS fluxes and resolved velocity gradients as outlined in §3.

Temporal averages of normalized forwardscatter and backscatter  $\langle \mathcal{P}_f \rangle, \langle \mathcal{P}_b \rangle / \langle -\tau_{ij} S_{ij} \rangle$  are shown versus the ratio  $\Lambda_w/\Delta_f$  in figure 14 (note that the sum of the normalized quantities equals unity). The most striking feature of figure 14 is that for values of the energy-filter ratio  $\Lambda_w/\Delta_f < 2$  the average backscatter is less than 20% and reaches a maximum of 50% at  $\Lambda_w/\Delta_f \approx 10$ . Also, we find

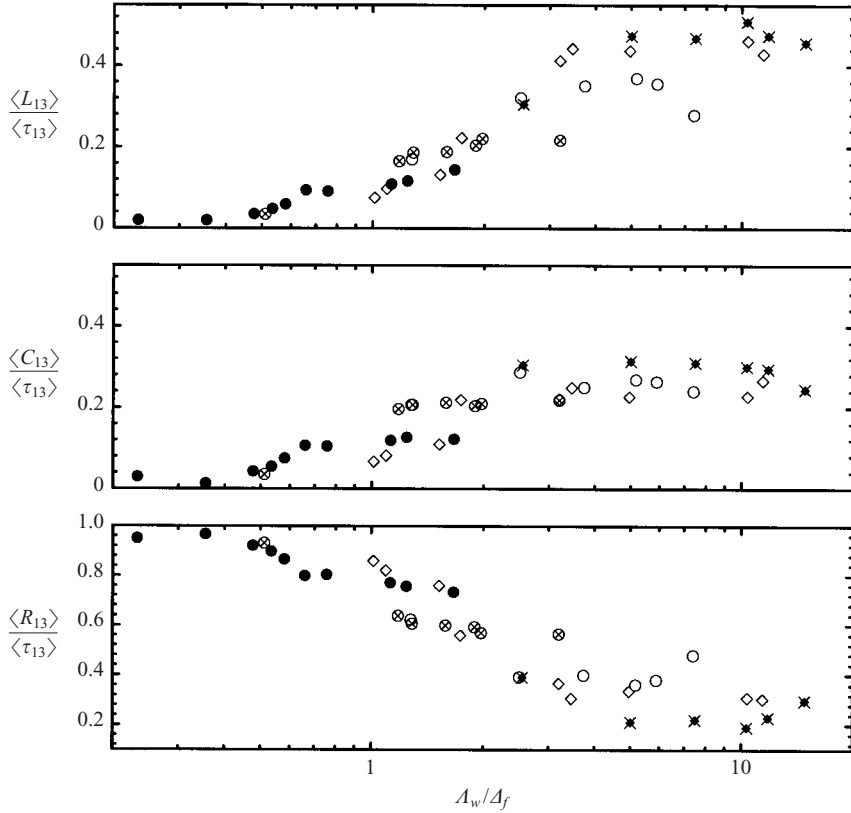


FIGURE 12. Decomposition of  $\tau_{13}$  flux into modified-Leonard, cross-, and Reynolds terms.

that the distribution of forwardscatter and backscatter events is similar to the partitioning of the energy, i.e. at  $\Lambda_w/\Delta_f = 2$  forwardscatter and backscatter occur roughly (80, 20)% of the time, respectively; the frequency of forwardscatter and backscatter is (65, 35)% at  $\Lambda_w/\Delta_f = 10$ . Figures 15 and 16 show the distribution of (normalized) forwardscatter and backscatter energy transfer amongst the three components ( $-L_{ij}S_{ij}$ ,  $-C_{ij}S_{ij}$ ,  $-R_{ij}S_{ij}$ ). At small  $\Lambda_w/\Delta_f$ , the energy transfer is entirely due to the SFS Reynolds term and is almost all forwardscatter. All three terms contribute equally to the forwardscatter at large energy-filter ratios, each reaching an asymptotic limit between 0.5 and 0.6. Meanwhile, the backscatter at  $\Lambda_w/\Delta_f = 10$  is equally distributed between the three SFS terms, each approaching  $-0.2$ . The contribution of the cross-term to the backscatter is perhaps slightly larger than the modified-Leonard and Reynolds terms at small  $\Lambda_w/\Delta_f$ . Based on these results, we conclude that the SFS motions do indeed induce backscatter of energy in the surface layer, but the magnitude of the process appears to be strongly scale dependent and hence its importance to SFS modelling depends on the resolution of LES. At the first few gridpoints above the surface, LES is in the range  $\Lambda_w/\Delta_f \leq 2$  and thus backscatter influences from the SFS motions are small. Backscatter of SFS energy is most important for well-resolved turbulence in the inertial range.

We note that our results are obtained using a mixed top-hat-Gaussian filter. Piomelli *et al.* (1991) found that the levels of plane-averaged ( $x, y$ ) forwardscatter and backscatter in a DNS of channel flow are higher for sharp spectral filters when

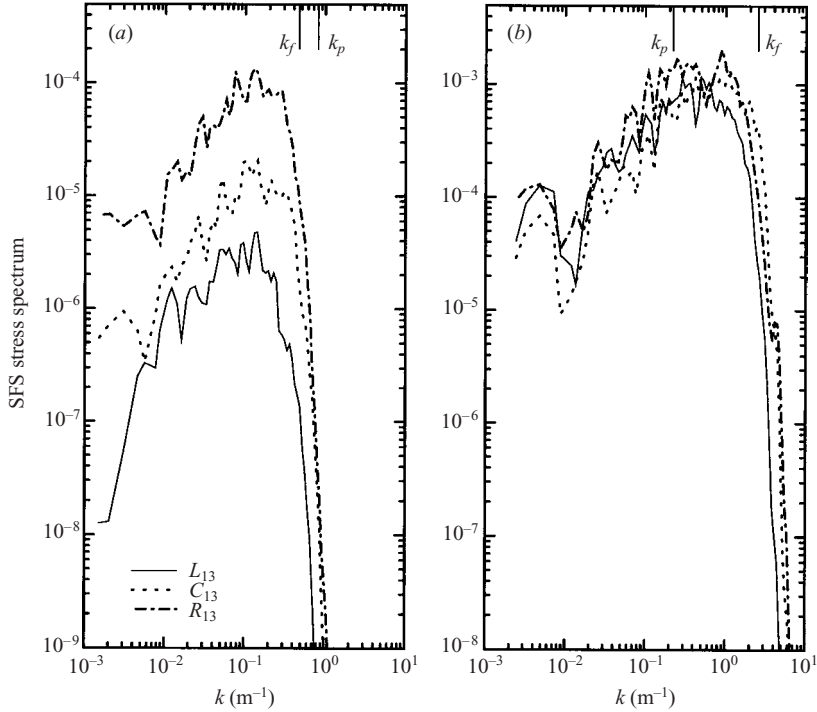


FIGURE 13. One-dimensional spectra of the SFS vertical momentum flux components ( $L_{13}$ ,  $C_{13}$ ,  $R_{13}$ ). (a) stable stratification with  $(\Lambda_w/\Delta_f) = 0.58$ , and (b) unstable stratification with  $(\Lambda_w/\Delta_f) = 11.4$ . Spectra are multiplied by the horizontal wavenumber  $k_1$  and normalized by  $\langle \tau_{13} \rangle^2$ . In each panel the locations of the peak and filter wavenumbers ( $k_p$ ,  $k_f$ ) are indicated by thin vertical lines.

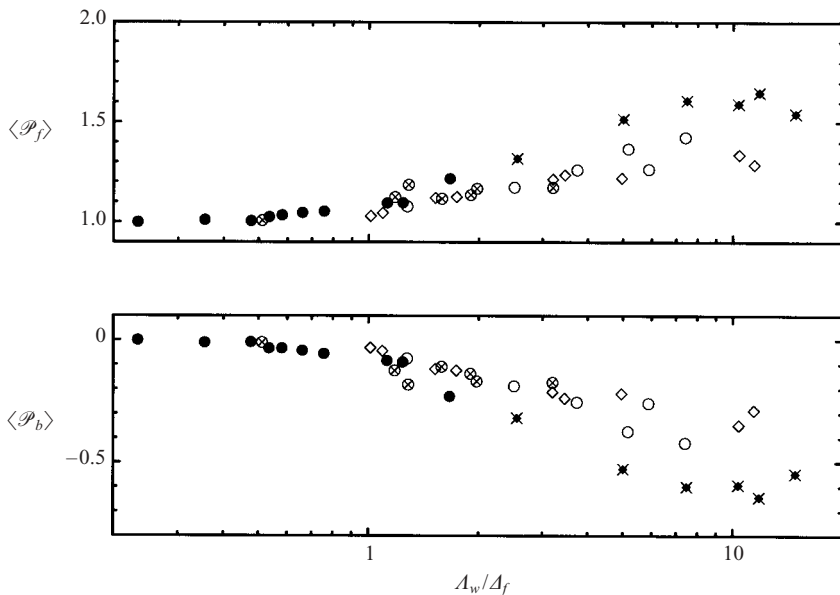


FIGURE 14. Production of SFS energy decomposed into forwardscatter  $\mathcal{P}_f$  and backscatter  $\mathcal{P}_b$  and normalized by the total production  $\langle -\tau_{ij}S_{ij} \rangle$  for varying  $\Lambda_w/\Delta_f$ .

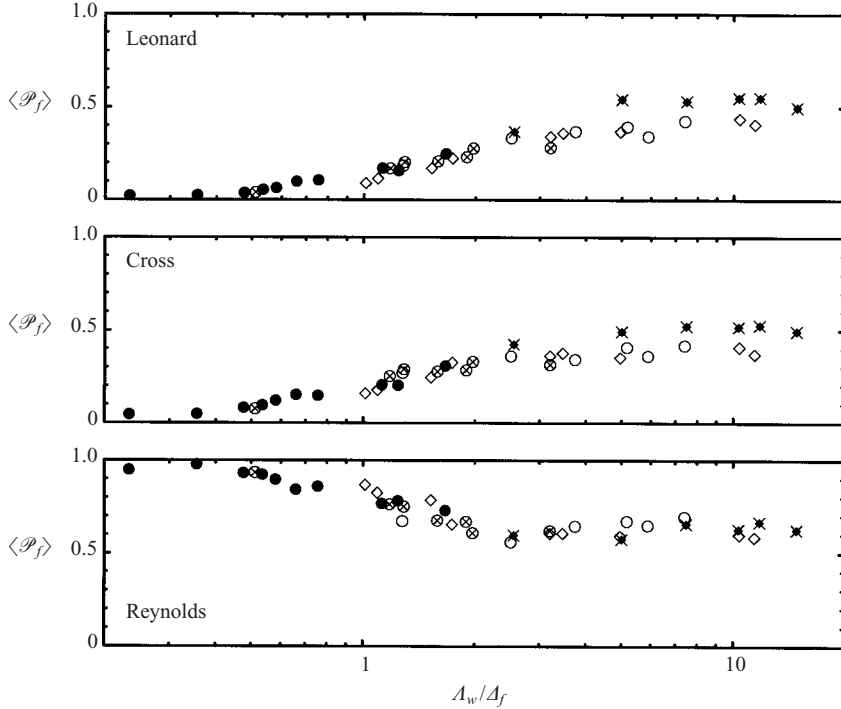


FIGURE 15. Forwardscatter of SFS energy normalized by the total SFS transfer  $\langle -\tau_{ij}S_{ij} \rangle$  by component for varying  $\Lambda_w/\Delta_f$ ; modified-Leonard  $\langle -L_{ij}S_{ij} \rangle$ , cross-  $\langle -C_{ij}S_{ij} \rangle$ , and Reynolds  $\langle -R_{ij}S_{ij} \rangle$  terms.

the ratio of SFS energy to total TKE is less than 5%, i.e. in our interpretation when  $\Lambda_w/\Delta_f \gg 1$ . For smaller cutoff wavenumbers (i.e. ratios of SFS energy to total TKE equal to 20%) their results are similar to those shown here.

## 6. *A priori* testing of SFS models

Low-Reynolds-number DNS data are traditionally used for SFS model evaluations since they contain the necessary three-dimensional spatial information to generate SFS fluxes and resolved field gradients. The ability to acquire multi-dimensional turbulence data in laboratory and field studies has, however, improved sufficiently that *a priori* testing can also now be performed with high-Reynolds-number measurements. There are many suggested SFS closures for LES and the testing of all such schemes is well beyond our scope. Here the HATS dataset is used to evaluate aspects of SFS models typical of those implemented in working LES of the PBL, many of which are eddy-viscosity-based parameterizations (e.g. Nieuwstadt *et al.* 1993; Sullivan *et al.* 1994). Alternative proposals for SFS models not based on an eddy-viscosity approach (e.g. Dubrulle *et al.* 2002; Zhou *et al.* 2001; Katopodes *et al.* 2000; Leonard 1997; and others) might also be evaluated with the HATS observations. We note that the *a priori* tests shown here are only a first step in judging a SFS model. *A posteriori* test with LES are required to ascertain the full interactions between resolved motions and the SFS model. Good performance of an SFS model in *a priori* tests does not always translate into acceptable LES. For example, the Bardina *et al.* (1983) model performs well in *a priori* tests but with no purely dissipative term is numerically unstable.

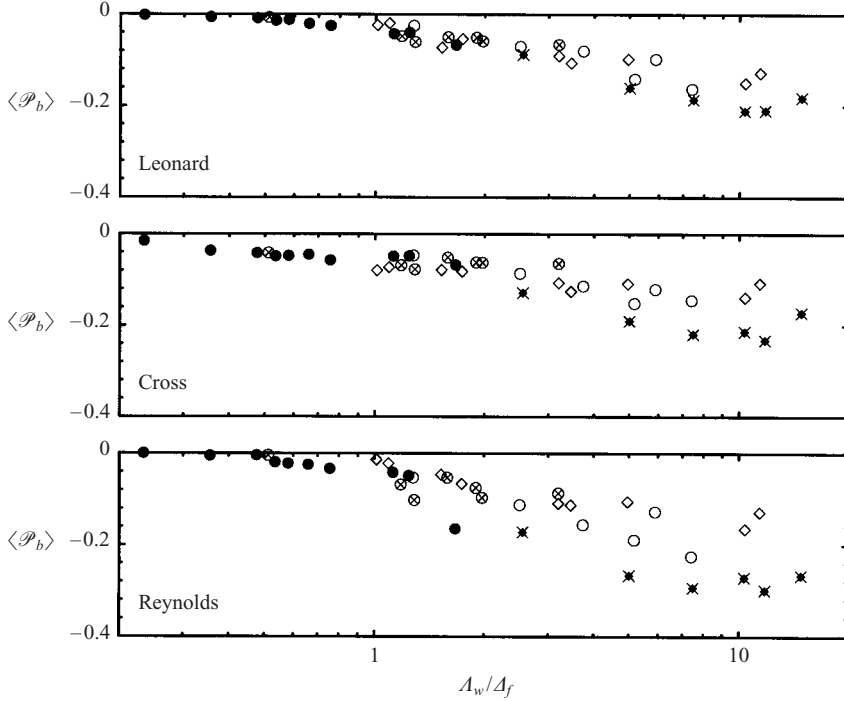


FIGURE 16. Backscatter of SFS energy normalized by the total SFS production  $\langle -\tau_{ij}S_{ij} \rangle$  by component for varying  $\Lambda_w/\Delta_f$ ; modified-Leonard  $\langle -L_{ij}S_{ij} \rangle$ , cross-  $\langle -C_{ij}S_{ij} \rangle$ , and Reynolds  $\langle -R_{ij}S_{ij} \rangle$  terms.

### 6.1. Eddy-viscosity model coefficients

We compute the SFS model coefficients  $C_k$  and  $C_s$  that appear in the TKE and Smagorinsky eddy-viscosity prescriptions described in the Appendix. Initially, a fixed length scale  $l = \Delta_f$  is used in the eddy viscosity; a length scale that is shear and stability dependent is considered in § 6.3. Average model coefficients are computed by equating the mean observed and modelled SFS energy production

$$\langle -\tau_{ij}^d S_{ij} \rangle \equiv \langle -\tau_{ij} S_{ij} \rangle = \langle 2\nu_t S_{ij} S_{ij} \rangle. \quad (6.1)$$

In (6.1),  $\tau_{ij} - \tau_{kk}\delta_{ij}/3$  is the deviatoric SFS flux tensor that appears in an LES formulation (see the Appendix),  $\nu_t = C_k l \sqrt{E_s}$  for the TKE model, and  $\nu_t = (C_s l)^2 |S|$  for the Smagorinsky parameterization. We also compute model coefficients by minimizing the difference  $(\tau_{ij}^d - \nu_t S_{ij})$  using least-squares and then time averaging. This alternative method produces values and trends similar to those found from (6.1).

The general variation of  $C_k$  and  $C_s$  with  $\Lambda_w/\Delta_f$ , shown in figures 17(a) and 18(a), is similar. The model coefficients tend towards an asymptote for large values of  $\Lambda_w/\Delta_f$  ( $C_s \approx 0.11$ ,  $C_k \approx 0.05$ ) and decrease sharply towards zero for  $\Lambda_w/\Delta_f < 2$ . Notice that our model coefficients at the largest available  $\Lambda_w/\Delta_f$  fall below the theoretical values of  $C_s = 0.17$  (Lilly 1967) and  $C_k = 0.094$  (Moeng & Wyngaard 1988; see also the Appendix). The important assumptions used in deriving these model coefficients are: sharp spectral filtering; a filter cutoff wavenumber,  $k_f = 2\pi/\Delta_f$ , in the inertial range of the turbulence; and an isotropic resolved-scale strain rate tensor. In the surface layer, these assumptions are violated to varying degrees. For the majority

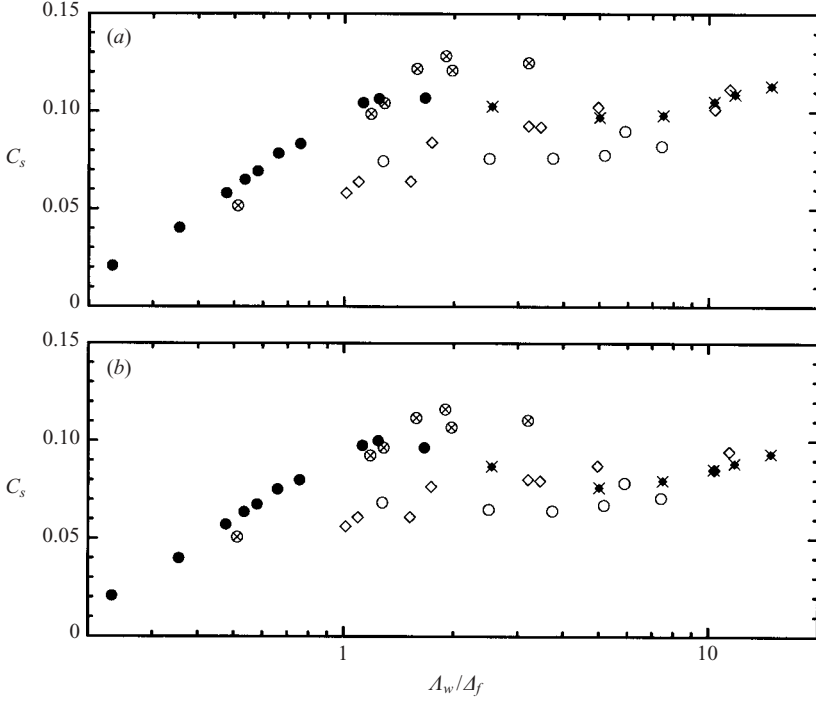


FIGURE 17. Smagorinsky coefficient  $C_s$  evaluated from SFS production with constant length scale  $l = \Delta_f$  for varying energy-filter ratio: (a) eddy-viscosity model and (b) mixed model.

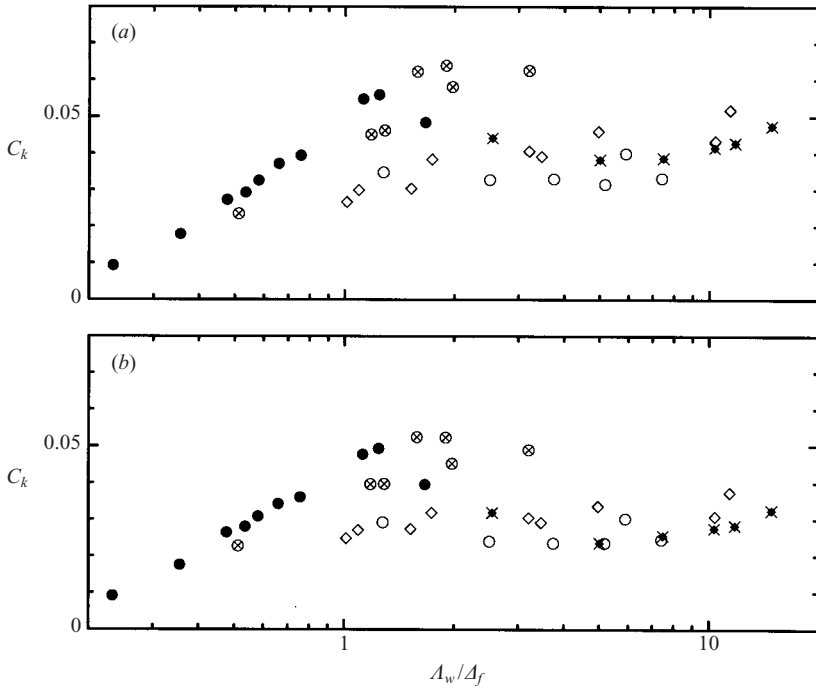


FIGURE 18. TKE coefficient  $C_k$  evaluated from SFS production with constant length scale  $l = \Delta_f$  for varying energy-filter ratio: (a) eddy-viscosity model and (b) mixed model.

of atmospheric stabilities, the filter-cutoff wavenumber separating the resolved and SFS is equal to or smaller than the wavenumber of the spectral peak in the vertical velocity, and hence  $k_f$  is smaller than the wavenumber where the inertial range begins. Also, our use of a two-dimensional top-hat Gaussian filter lowers the estimates of  $C_k$  (see the Appendix). Finally, since the SFS variances are not isotropic, it is expected that the resolved strain rates are similarly anisotropic. Therefore, the SFS coefficients obtained from the measurements and the theoretical analysis differ. Observations at or near the top of the surface layer, under unstable buoyancy forcing, would yield  $\Lambda_w/\Delta_f \gg 20$ , and then the SFS motions would probably conform more closely to the assumptions of the theoretical analysis.

For  $\Lambda_w/\Delta_f < 2$ , the Smagorinsky coefficient  $C_s \propto \kappa z/\Delta_f$ , where  $\kappa$  is the von Kármán constant (Pope 2000, p. 597). Porté-Agel *et al.* (2001) also reported that the value of  $C_s$  decreased to values as low as 0.06 for small  $z/\Delta_f$ ; for constant atmospheric stability,  $z/\Delta_f \propto \Lambda_w/\Delta_f$ . In LES, small values of  $\Lambda_w/\Delta_f$  result from stable stratification, close proximity to the surface, or large grid spacings (or a combination of the three), see figure 4. Note that in QDNS,  $C_s$  decreases at a faster rate near the wall because of the viscous sublayer (Germano *et al.* 1991).

We observe that the model coefficients in figures 17(a) and 18(a) tend to cluster into groups by array configuration as  $\Lambda_w/\Delta_f$  varies. This behaviour coupled with the dependence of the model coefficients on  $\Lambda_w/\Delta_f$  suggests that the TKE and Smagorinsky models neglect important physical effects since the SFS fluxes (see §5) collapse reasonably well across the range of  $\Lambda_w/\Delta_f$  considered. Hence, proposing a general parameterization for  $C_s$  and  $C_k$  in the surface layer from these results is not attractive. Our measurements are consistent with past experience that the value of the Smagorinsky coefficient must be reduced from its theoretical value, by as much as a factor of 2, to sustain near-wall turbulence and generate realistic simulations of neutral boundary layers (e.g. Deardorff 1970; Moin & Kim 1982; Sullivan *et al.* 1994). For example, at the first grid point above the surface for a neutral boundary layer,  $\Lambda_w/\Delta_f \approx 1$  (figure 4) and the corresponding  $C_s \approx 0.08$  from figure 17(a).

## 6.2. Mixed SFS model

The modified-Leonard term is an important component of the SFS tensor (1.2) and is responsible for a significant fraction of the SFS energy production (see §§5.3 and 5.4). At the same time,  $L_{ij}$  depends only on the resolved-scale velocity which can be accounted for directly in SFS models. However, a parameterization for the cross- and Reynolds terms is still required since their contribution to  $\tau_{ij}$  is non-negligible for all  $\Lambda_w/\Delta_f$  (see §5). Hence, we next consider a so-called mixed model for the SFS flux of the form

$$\tau_{ij}^d = L_{ij}^d - 2\nu_t S_{ij}, \quad (6.2)$$

where now  $-2\nu_t S_{ij}$  is interpreted as a parameterization for the deviatoric SFS flux  $(C_{ij} + R_{ij})^d$ .

From an implementation perspective, (6.2) is equivalent to the mixed models first proposed by Bardina *et al.* (1983), but the steps leading to (6.2) differ. The Galilean-invariant decomposition of the SFS tensor (1.3) and the need to model the cross- and Reynolds SFS stress tensors naturally lead to (6.2). Bardina *et al.* (1983) and others have shown that a similarity model alone, i.e.  $\tau_{ij} = L_{ij}$ , does not generate sufficient SFS dissipation when implemented in LES and thus an explicit diffusion term is required. Our results in §5 confirm that while  $L_{ij}$  is significant  $\tau_{ij} \neq L_{ij}$ . In *a posteriori* tests, Vreman, Guerts & Kuerten (1997) found that the mixed model with a dynamic estimation of the eddy-viscosity coefficient yielded the most accurate LES of

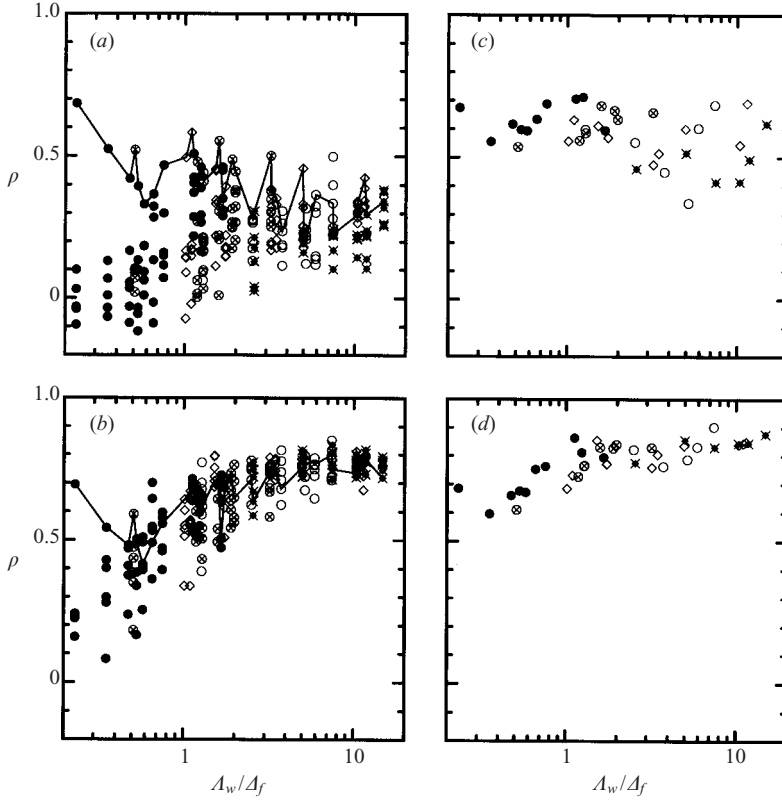


FIGURE 19. Correlations between TKE model and observations for varying energy-filter ratio and constant length scale  $l = \Delta_f$ : (a) eddy viscosity model for  $\tau_{ij}^d$ ; (b) mixed model for  $\tau_{ij}^d$ ; (c) eddy viscosity model for  $\tau_{ij} S_{ij}$ ; and (d) mixed model for  $\tau_{ij} S_{ij}$ . In (a) and (b) the correlation for the (1,3) component of the SFS flux ( $\tau_{13}^d$ ) is shown as a solid line.

a turbulent mixing layer while Liu *et al.* (1994) found that a mixed model correlated well with experimental data for a round jet. On the other hand, Juneja & Brasseur (1999), using DNS data, found that a similarity model did not perform as well in *a priori* tests of homogeneous turbulence when the filter cutoff encroached into the energy containing range of the turbulence.

The objective here is to investigate the properties of a mixed model as applied to SFS turbulence near a rough wall. By analogy with (6.1), we use

$$\langle \tau_{ij} S_{ij} - L_{ij} S_{ij} \rangle = \langle -2v_t S_{ij} S_{ij} \rangle \quad (6.3)$$

to compute the SFS model coefficients  $C_k$  and  $C_s$  for  $l = \Delta_f$ . The results are displayed in figures 17(b) and 18(b). The impact of including  $L_{ij}$  explicitly is to reduce the predicted values of the SFS coefficients at large values of  $\Lambda_w/\Delta_f$ ; this is more significant for the TKE model coefficient (figure 18b). The reduction is expected since  $L_{ij}$  is a significant contributor to the total SFS flux only at large values of  $\Lambda_w/\Delta_f$  (see figures 9–12). Disappointingly, the scatter in the model coefficients and their systematic variation with  $\Lambda_w/\Delta_f$  is only reduced slightly by comparison to the results in figures 17(a) and 18(a).

While the impact of  $L_{ij}$  on the average model coefficients is small, its influence on the correlations between modelled and observed SFS flux is significant. Figure 19 shows

correlation coefficients for individual components of the SFS flux  $\tau_{ij}^d$  and SFS energy transfer  $\tau_{ij}S_{ij}$  using the TKE model (results are similar for the Smagorinsky model). Correlations are shown both with the modified-Leonard term included (mixed model) and without it (eddy-viscosity model). Here the correlation coefficient is defined as

$$\rho(a, b) = \frac{\langle ab \rangle - \langle a \rangle \langle b \rangle}{\sqrt{\langle a^2 \rangle - \langle a \rangle^2} \sqrt{\langle b^2 \rangle - \langle b \rangle^2}}, \quad (6.4)$$

where  $(a, b)$  are observed and modelled variables, respectively.

In the absence of  $L_{ij}$  (see figure 19a), the correlations between measured and modelled  $\tau_{ij}^d$  are less than 0.5 over the entire range of energy-filter ratios; negative correlations are found at low values of  $\Lambda_w/\Delta_f$ , further exposing the inadequacy of an eddy-viscosity relationship. The highest correlation ( $\rho \approx 0.45$ ) between modelled and observed SFS flux occurs for  $\tau_{13}$ ; this correlation is shown as the solid line in figure 19(a). As  $\Lambda_w/\Delta_f \rightarrow 0$ , a flux–gradient relationship exists for the (1, 3)-component of the SFS flux and strain rate as they tend to their ensemble average values,  $\tau_{13} \rightarrow \langle uw \rangle$  and  $S_{13} \rightarrow \partial \langle U \rangle / \partial z$ . The correlation between modelled and measured SFS energy transfer with the eddy-viscosity model (see figure 19c) is generally higher than for the individual flux components. This is also found with *a priori* tests using DNS databases and illustrates that the primary success of an eddy-viscosity model is to generate reasonable amounts of average energy transfer between resolved and SFS scales in simulations (see Meneveau & Katz 2000).

With the mixed model (figure 19b), the correlations between all components of the modelled and observed fluxes approach 0.8 or higher for large  $\Lambda_w/\Delta_f$ . This is consistent with our analysis of the SFS tensor which showed that the magnitude and spectral content of  $L_{ij}$  is comparable to  $C_{ij}$  and  $R_{ij}$  (see § 5). At small  $\Lambda_w/\Delta_f$ , higher correlations are clearly observed in figure 19(b) compared to those in figure 19(a). Examination of the SFS energy production in figure 19(d) shows that explicit  $L_{ij}$  in the mixed model raises the correlation to values approaching 0.9 for all combinations of filter widths and atmospheric stability. In addition, the correlations collapse reasonably well in figure 19(d). The elevated correlations for SFS energy production reflect the importance of  $L_{ij}S_{ij}$  to the SFS energy transfer; it accounts for at least 30% of the average energy transfer at  $\Lambda_w/\Delta_f = 10$ . In addition,  $L_{ij}S_{ij}$  allows for both forwardscatter and backscatter of energy which also contributes to higher correlations for the SFS energy production.

### 6.3. Shear- and stability-corrected length scale

The mixed model (6.2) produces significantly improved correlations between the modelled and observed SFS fluxes and energy transfer compared to a pure eddy-viscosity model. However, the coefficient  $C_k$  (or  $C_s$ ) in the eddy-viscosity term of the mixed model still retains a dependence on the energy-filter ratio, especially when the modified-Leonard term is small. Note the marked decrease of  $C_k$  and  $C_s$  for small values of  $\Lambda_w/\Delta_f$  in figures 17(b) and 18(b). When the filter cutoff wavelength is at or near the peak in the vertical velocity spectrum, the SFS turbulence is strongly non-inertial and influenced by stable stratification, large-scale shear and the proximity of the lower surface; these effects need to be included in an eddy-viscosity prescription.

Deardorff (1980), Schumann (1991), Hunt, Stretch & Britter (1988), Yoshizawa (1998), and others propose SFS models that attempt to incorporate large-scale shear and stable stratification. Both influences are also important ingredients in our current SFS model (see the Appendix and Sullivan *et al.* 1994). The adequacy of all these parameterizations for SFS fluxes remains relatively untested however.

All these proposals are of a similar form and essentially introduce a variable eddy-viscosity length scale  $l$  that depends on the large-scale shear  $|S| = \sqrt{2S_{ij}S_{ij}}$  and the stratification through the Brunt–Väisälä frequency  $N^2 = (g/\theta_0)(\partial\theta/\partial z)$ . Canuto & Cheng (1997) performed a thorough theoretical study of the effects of shear and stability on the length scale and proposed a correction that systematically includes both effects. The critical step in their analysis is construction of an energy spectrum in the presence of buoyancy and shear which then makes the length scale  $l$  dependent on  $(|S|, N)$  through the SFS energy. Their model for  $l$  is attractive since it is more general than prior studies; it also reduces to the Hunt *et al.* (1988) proposal in the limit of neutral flow and approaches Deardorff's model (see the Appendix) for large stratification. Deardorff's model is ill-behaved near neutral stratification.

The Canuto & Cheng (1997) length-scale model is of the form  $l = f(|S|, N)\Delta_f$  where their expression for the length-scale correction in equilibrium flow is

$$f(|S|, N)^{2/3} = \int_0^1 [1 - b \ln(1 + aq^2)]^2 dq, \quad (6.5)$$

with the definitions

$$b = \frac{\sqrt{3}}{16} K_o^{3/2} \left( \frac{Pr_t Sh^2}{Fi^2} - 1 \right), \quad a = \frac{2}{\pi^2} Fi^2 f(|S|, N)^{2/3}, \quad q = \left( \frac{k}{k_m} \right)^{2/3}, \quad k_m = \frac{\pi}{\Delta_f}. \quad (6.6)$$

In (6.6), the non-dimensional shear and inverse Froude numbers are  $Sh = \Delta_f |S| / \sqrt{E_s}$  and  $Fi = \Delta_f N / \sqrt{E_s}$ , the Kolmogorov constant  $K_o = 1.5$ , and  $Pr_t$  is the turbulent Prandtl number. A power series expansion of the integral in (6.5) for small  $Fi$  leads to the following expression for neutral flow:

$$f(|S|)^{2/3} = \int_0^1 [1 - b'q^2]^2 dq, \quad (6.7)$$

with

$$b' = \frac{\sqrt{3}}{8\pi^2} K_o^{3/2} Pr_t Sh^2 f(|S|). \quad (6.8)$$

The length-scale correction given by (6.5) depends on the particular combination of shear, stratification, and filter width. To evaluate (6.5) as a length-scale parameterization we compute time series of  $Sh$  and  $Fi$  using instantaneous values of  $\partial\bar{U}_i/\partial x_j$ ,  $\partial\bar{\theta}/\partial z$ , and  $E_s$ .  $Fi$  is evaluated at all points with stable stratification and otherwise  $Fi = 0$ . Figure 20 shows the variation of the average shear,  $\langle Sh \rangle$ , and stratification,  $\langle Fi \rangle$ , for varying atmospheric conditions in the surface layer. For  $z/L$  in the range  $[-1, 2]$ , the  $\langle Sh \rangle$  varies in the range  $[4, 22]$  and  $\langle Fi^{-1} \rangle$  in the range  $[0.01, 8]$ . When  $z/L < 0$ ,  $\langle Sh \rangle$  becomes nearly independent of stratification and approaches a constant  $\approx 4$ . This behaviour can be understood by examining  $Sh$  for large  $\Lambda_w/\Delta_f$  and  $z/L < 0$ ; we find that  $|S| \sim \Delta_f^{-2/3}$ ,  $E_s \sim \Delta_f^{2/3}$  and hence  $\Delta_f |S| / \sqrt{E_s}$  tends to a constant. When  $z/L < 0$ ,  $Fi$  is small and thus the length-scale correction depends only on shear. As the atmosphere becomes increasingly stable,  $Fi$  and  $Sh$  both increase with  $z/L$ , more so for cases with large filter widths. As a result, the length-scale correction depends strongly on both  $|S|$  and  $N$  for stably stratified flows.

In order to utilize (6.5) as a length-scale model we also need to specify the turbulent Prandtl number in addition to computing  $Sh$  and  $Fi$  at each point in the time series. For our evaluation, we adopt the Deardorff (1980) model (A 6) which makes  $Pr_t$  a function of the length-scale correction  $f$ . With this model, the range of  $Pr_t$  is  $[0.3, 1]$

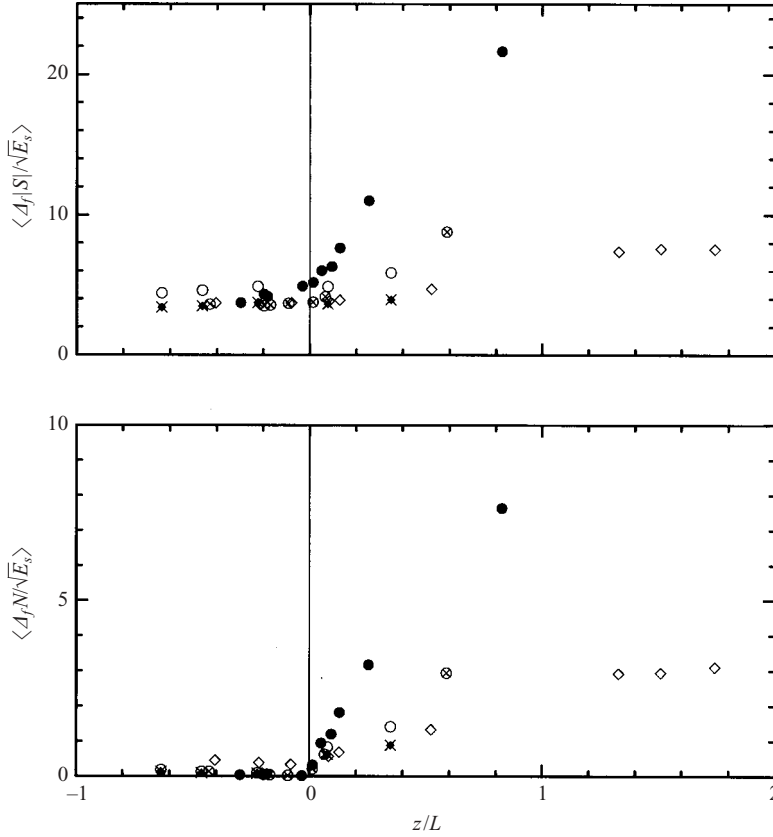


FIGURE 20. The variation of the non-dimensional shear and stratification with atmospheric stability  $z/L$ . The shear number  $Sh = \Delta_f |S| / \sqrt{E_s}$  and the inverse Froude number  $Fi = \Delta_f N / \sqrt{E_s}$ .

for  $f = [1, 0]$ . Integrals (6.5) and (6.7) cannot be evaluated in closed form because of the kernel dependences on  $f$ . A Simpson's rule quadrature and an iterative method based on interval-halving are used to obtain numerical values of  $f$  from (6.5) when  $Fi > 0.01$  and (6.7) for  $Fi < 0.01$ .

Figure 21 shows the variation of the average length-scale factor  $\langle f(|S|, N) \rangle$  across the range of energy-filter ratios. At large  $\Lambda_w / \Delta_f$ ,  $f$  approaches a constant as the influence of stratification is negligible ( $Fi \approx 0$ ) and  $Sh$  tends to its asymptotic value. Note that with this length-scale prescription, there is always a small correction due to shear even at very large  $\Lambda_w / \Delta_f$  (this makes  $f$  vary smoothly as  $Sh$  changes). As the energy-filter ratio decreases,  $Sh$  and  $Fi$  both increase which results in significant reduction in  $f$  and hence the length scale  $l$ . The length-scale correction variation also depends slightly on the array configuration since  $Sh$  and  $Fi$  are functions of the filter width and the specific atmospheric conditions.

Values of the eddy-viscosity coefficients  $C_k$  and  $C_s$  from the mixed model (6.2) with the shear-stability-dependent length scale  $l = f \Delta_f$  are shown in figure 22. Compared to the results obtained with  $l = \Delta_f$  (see figures 17 and 18), the length-scale correction has removed a large fraction of the  $C_k$  and  $C_s$  dependence on  $\Lambda_w / \Delta_f$ . Inspection of (6.2) shows that if  $l$  decreases in the eddy-viscosity term then the model coefficient ( $C_k$  or  $C_s$ ) must increase. We estimate average values of the model coefficients as

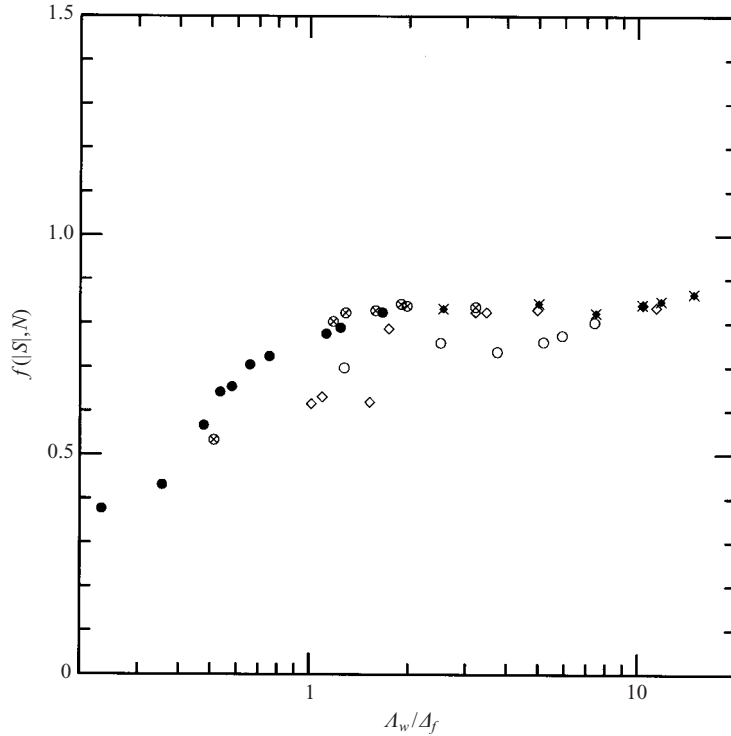


FIGURE 21. The shear and stability corrected length scale factor from Canuto & Cheng (1997) for varying  $A_w/\Delta_f$ .

$C_s \approx 0.11$  and  $C_k \approx 0.045$ . The correlations between observed and modelled SFS fluxes and energy production using the mixed model and a shear-stability-dependent length scale  $l = f \Delta_f$  are improved slightly by comparison to the correlations obtained with a constant length scale  $l = \Delta_f$  (results not shown). Further improvements to the modelling can perhaps be obtained by using a more general stress-strain relationship, i.e. a nonlinear eddy-viscosity model (Canuto & Cheng 1997).

#### 6.4. Dissipation model

The SFS dissipation parameterization is a critical aspect of our TKE model (see the Appendix). Moeng & Wyngaard (1988) show that for filter cutoff wavenumbers in the inertial range the SFS energy and filter width must vary in a lock-step fashion ( $E_s \sim \Delta_f^{2/3}$ ) so that the average dissipation for a particular flow remains constant. In view of the non-inertial SFS motions in the surface layer, it is then important to examine the validity of this dissipation parameterization for changing filter width and atmospheric stability.

The spatial resolution of a sonic anemometer does not allow direct measurement of viscous dissipation and thus we need a surrogate to compare with a dissipation parameterization. Here we assume that the measured SFS energy transfer  $\mathcal{P}$  is equal to the dissipation  $\epsilon$  and evaluate the dissipation parameterization (A 4) based on the assumption

$$-\tau_{ij} S_{ij} = C_\epsilon \frac{E_s^{3/2}}{l}, \quad (6.9)$$

where  $C_\epsilon$  is the dissipation coefficient.

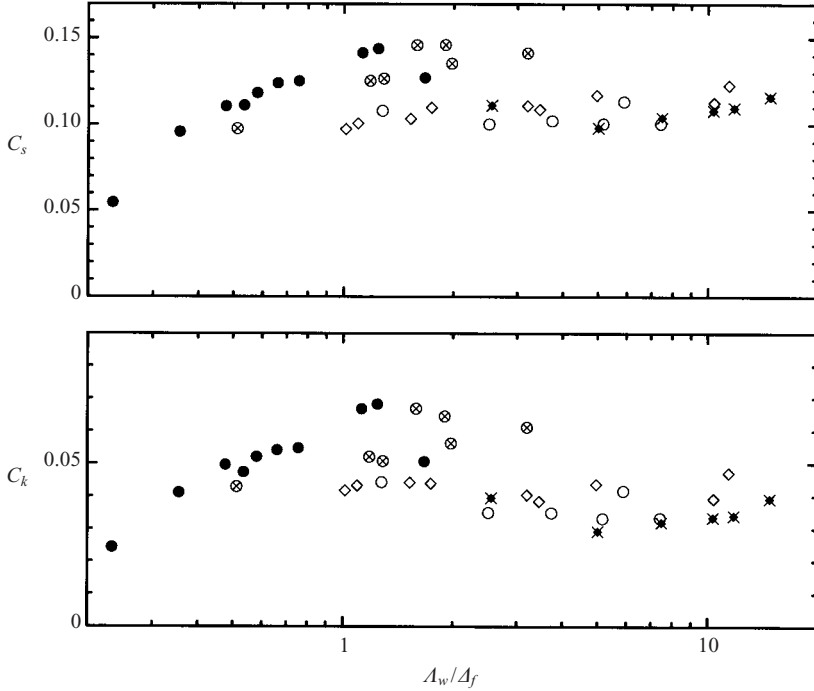


FIGURE 22. Smagorinsky and TKE coefficients in a mixed SFS model with shear and stability corrected length scale  $l = f \Delta_f$  as function of the energy-filter ratio.

Contours of the joint probability density function of the measured SFS energy production and the modelled dissipation are shown in figure 23 for three values of  $\Lambda_w/\Delta_f$ . In this comparison,  $l = \Delta_f$  and we use  $C_\epsilon = 0.66$  appropriate for Gaussian filtering (Note that  $C_\epsilon = 0.93$  for a sharp spectral cutoff filter; see the Appendix). Values are normalized by the average SFS energy production  $\langle \mathcal{P} \rangle$ . These cases are selected since they illustrate the changing behaviour of the dissipation parameterization as the energy-filter ratio varies. For  $\Lambda_w/\Delta_f = 0.23$  (figure 23a) and  $\Lambda_w/\Delta_f = 0.58$  (figure 23b) the standard dissipation parameterization is too small on average compared to the observed  $\mathcal{P}$ , whereas at large energy-filter ratios ( $\Lambda_w/\Delta_f = 11.4$ ; figure 23c), the SFS production and parameterized dissipation are in approximate balance on average. Also, notice that the probability density contours spill over into negative regions of SFS energy production. This backscatter of energy from the SFS motions to the resolved scales, as shown earlier, is most significant for large  $\Lambda_w/\Delta_f$ . The positive-definite dissipation parameterization (A 4) is unable to capture this effect. Also apparent from these contours is the increased fluctuation level in SFS energy production and hence dissipation with increasing  $\Lambda_w/\Delta_f$  – the contours for  $\Lambda_w/\Delta_f = 11.4$  clearly extend to larger  $\epsilon$  values than for  $\Lambda_w/\Delta_f = 0.23$  (figure 23a).

By trial and error, Deardorff (1973) determined that  $C_\epsilon = 0.7$  yielded realistic simulations. This choice is consistent with our analysis in the Appendix that shows that the dissipation coefficient is lower for Gaussian filtering; such filtering is a reasonable approximation for a finite-difference code. The results in figure 23, however, indicate a more general dependence on the energy-filter ratio. To quantify this dependence, we compute the dissipation coefficient by averaging (6.9) using the length scales  $l = \Delta_f$

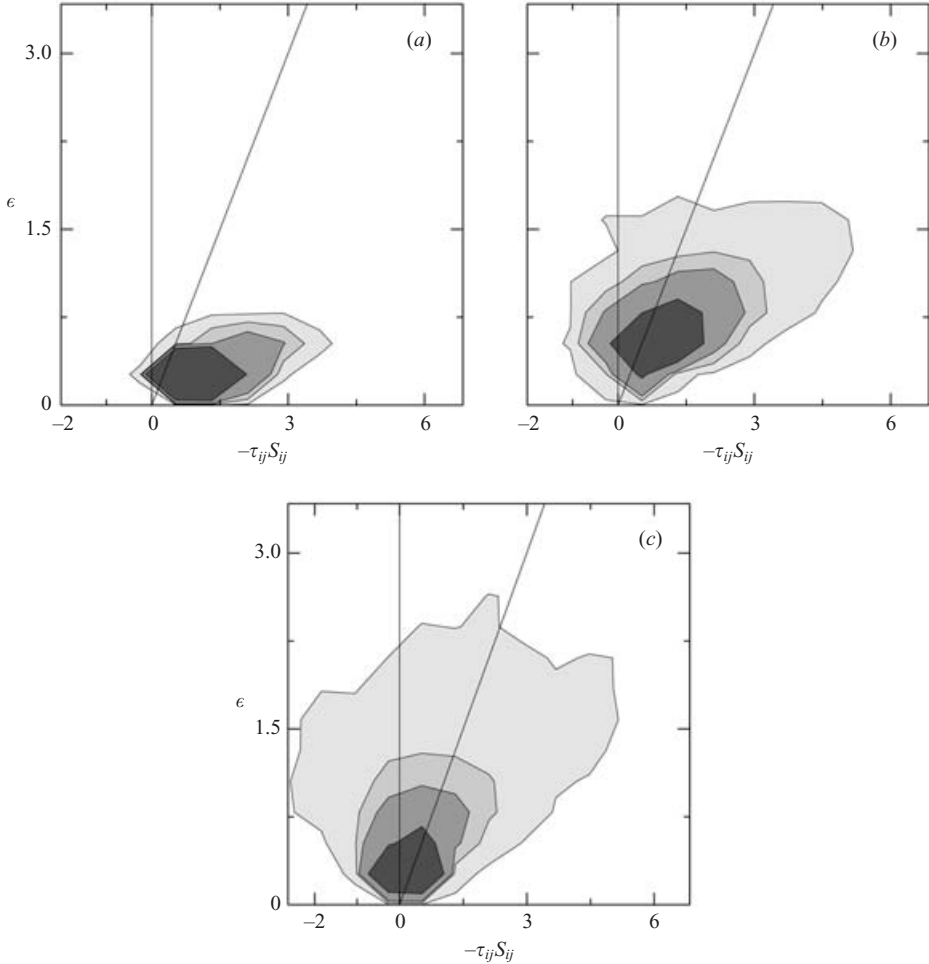


FIGURE 23. Contours of the joint probability distribution of the model dissipation  $\epsilon = C_\epsilon E_s^{3/2}/l$  and the measured SFS energy production  $-\tau_{ij} S_{ij}$ .  $\epsilon$  and  $-\tau_{ij} S_{ij}$  are normalized by the average production  $\langle -\tau_{ij} S_{ij} \rangle$  and  $(C_\epsilon, l) = (0.66, \Delta_f)$ . The shading darkens with decreasing contour values (0.008, 0.05, 0.1, 0.35). (a)  $(z/L, \Lambda_w/\Delta_f) = (0.82, 0.23)$ ; (b)  $(0.05, 0.58)$ ; and (c)  $(-0.40, 11.4)$ . The sloping line corresponds to  $\epsilon = -\tau_{ij} S_{ij}$ . Energy backscatter occurs at all points where  $-\tau_{ij} S_{ij} < 0$ .

and  $l = f \Delta_f$  for each measurement period. The results are displayed in figure 24. For constant  $l = \Delta_f$  (see figure 24a),  $C_\epsilon \approx 0.66$  for  $\Lambda_w/\Delta_f \approx 3$  or greater, but  $C_\epsilon$  exhibits a sharp increase for very small values of  $\Lambda_w/\Delta_f$ . At large energy-filter ratios, the filter-cutoff wavenumber is encroaching into the inertial range where  $\epsilon$  is a constant. Our measurements suggest an asymptote of  $C_\epsilon = 0.5$ – $0.6$  which supports Deardorff's dissipation coefficient of 0.7.

The impact of including a variable length scale (see figure 24b) is to lower  $C_\epsilon$  and to eliminate much of the variation with  $\Lambda_w/\Delta_f$ . This is expected since the variable length scale also produced reasonably constant values of the TKE and Smagorinsky coefficients. However, a persistent trend for  $C_\epsilon$  to increase with decreasing  $\Lambda_w/\Delta_f$  still exists. Further analysis and modelling are required to understand and parameterize this trend.

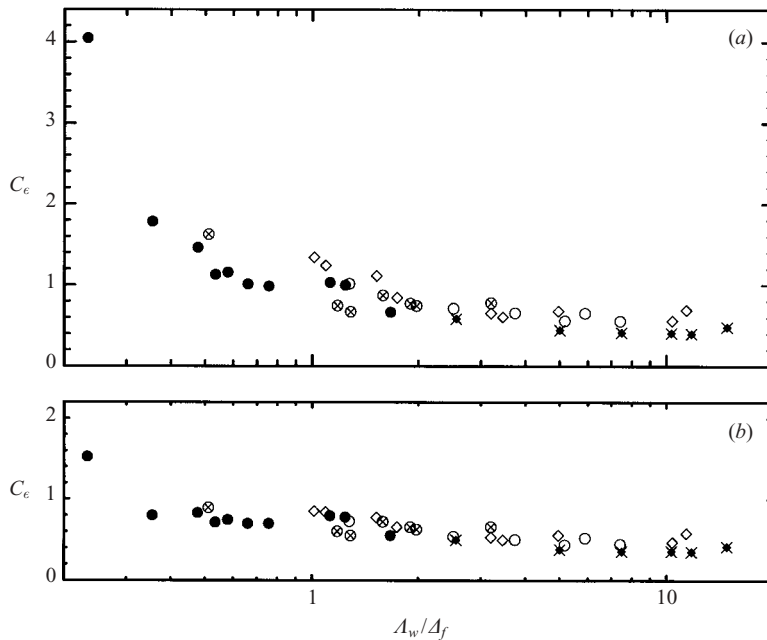


FIGURE 24. Dissipation coefficient  $C_e$  evaluated by matching the average model dissipation and SFS production: (a) constant length scale  $l = \Delta_f$  and (b) variable length scale  $l = f \Delta_f$ .

## 7. Conclusions

The structure of the subfilter-scale (SFS) turbulent motions in the atmospheric surface layer is sensitive to the relative positions of the spectral peak of the vertical velocity  $\Lambda_w$  and the filter cutoff scale  $\Delta_f$ .  $\Lambda_w$  decreases with increasing stability and decreasing vertical distance from the surface, and this dependence constrains our ability to perform large-eddy simulation (LES). As the grid resolution is refined, both the LES filter cutoff  $\Delta_{f,les}$  and  $\Lambda_w$  at the first grid level ( $\delta z$ ) shift proportionally to smaller scales, i.e.  $\Delta_{f,les}$  cannot be moved independently of  $\Lambda_w$  (at  $z = \delta z$ ). As a result, the SFS fluxes in LES are always significant at the first grid level and their contribution to the total flux grows with increasing stability. For LES with  $200^3$  gridpoints,  $\Lambda_w/\Delta_{f,les}$  is approximately in the range  $[0.1, 20]$  in the surface layer.

Measurements of SFS fluxes and variances from the Horizontal Array Turbulence Study (HATS) field program collapse reasonably well when plotted as a function of the energy-filter ratio  $\Lambda_w/\Delta_f$ . This holds true for  $\Lambda_w/\Delta_f$  over the broad range  $[0.2, 15]$  and includes a wide variety of stratifications and filter widths. In the surface layer, the SFS variances are anisotropic and the SFS energy is non-inertial, and they exhibit a strong dependence on the stratification, large-scale shear, and proximity to the surface – more so for small  $\Lambda_w/\Delta_f$ . At  $\Lambda_w/\Delta_f \approx 1$ , the SFS fluxes ( $\tau_{11}$ ,  $\tau_{22}$ ,  $\tau_{33}$ ,  $\tau_{13}$ ) contribute at least (40, 40, 90, 75)% to the respective total fluxes. The fractional contribution is even greater for slight increases in stability.

Decomposition of the SFS flux into modified-Leonard, cross-, and Reynolds terms shows that these terms are of comparable magnitude and scale content at large  $\Lambda_w/\Delta_f$ . The modified-Leonard term is equivalent to the Bardina *et al.* (1983) scale-similarity term. As  $\Lambda_w/\Delta_f$  decreases, the SFS flux approaches the ensemble average and is dominated by the Reynolds term. Computations of SFS energy production show that the backscatter of energy from the SFS motions to the resolved fields is

less than 20% for  $\Lambda_w/\Delta_f < 2$ . Energy backscatter in LES is most important for well-resolved turbulence exhibiting an inertial range, e.g. at the top of the surface layer. Hence, in the surface layer, the inclusion of energy backscatter in an SFS model is not crucial for small  $\Lambda_w/\Delta_f$  values. The SFS energy production from the modified-Leonard term amounts to at least 30% of the total, contains both forwardscatter and backscatter of energy, and can be computed directly with resolved-scale information.

*A priori* testing of SFS models with the HATS dataset shows that the turbulent kinetic energy and Smagorinsky model coefficients  $C_k$  and  $C_s$ , derived from the measurements, depend on  $\Lambda_w/\Delta_f$  and are smaller than the theoretical estimates based on the assumption of a sharp spectral cutoff in the inertial range. With stable stratification or small height  $z$  (small  $\Lambda_w/\Delta_f$ ), the measured  $C_k$  and  $C_s$  tend to zero. For a pure eddy-viscosity model, the correlations between measured and observed SFS fluxes and energy transfer are relatively low, but mixed SFS models that explicitly include the modified-Leonard term exhibit much higher correlations. However, even with the mixed model, the eddy-viscosity model coefficients retain a significant dependence on  $\Lambda_w/\Delta_f$ . Much of this dependence is removed by including a shear-stability length-scale parameterization (Canuto & Cheng 1997) in the eddy-viscosity model. Furthermore, this parameterization improves the behaviour of the coefficient  $C_\epsilon$  in a dissipation model,  $\epsilon = C_\epsilon E_s^{3/2}/l$ , used in SFS modelling, i.e. the  $C_\epsilon$  based on the variable length scale  $l$  exhibits substantially less variation with  $\Lambda_w/\Delta_f$  than the  $C_\epsilon$  for a constant  $l(=\Delta_f)$ . Finally, we note that the definition of filter width  $\Delta_f$  used in the data analysis cannot be equated exactly with the filter width  $\Delta_{f,les}$  used in LES boundary layer codes. The latter is imprecisely known, varying with the numerical method and proximity to the boundary.

In summary, for neutral and stable surface-layer flows, the difficulty of performing LES with a standard Smagorinsky model can be explained by: (i) the increasing dominance of the SFS motions with increasing stability, (ii) the departure of the SFS motions from the classical view of inertial-range turbulence, and (iii) the inability to vary the filter cutoff independently of the peak in the energy spectrum.

We wish to thank Jan Kleissl, Charles Meneveau Marc Parlange of Johns Hopkins University for their enthusiastic and helpful participation in the HATS field program and for their insights into the data analysis. Chenning Tong and John Finnigan willingly shared their experiences on practical matters associated with the field measurements. The anonymous reviewers provided helpful comments on a draft of the manuscript. Special thanks go to John Wyngaard for his encouragement to pursue this research topic. P.P.S. was partially supported by the Office of Naval Research through the CBLAST initiative, contract N00014-00-C-0180, and the NASA Land Surface Hydrology Program, grant number NAG5-8839. J.C.W. was supported by the US Army Research Office under contract DAAG-55-91-1-0259. NCAR is sponsored by the National Science Foundation.

## Appendix. TKE and Smagorinsky SFS models

In LES, the normal SFS stress  $\tau_{kk}$  is absorbed in the effective pressure and a parameterization of the deviatoric SFS flux,

$$\tau_{ij}^d = \tau_{ij} - \frac{1}{3}\tau_{kk}\delta_{ij}, \quad (\text{A } 1)$$

is required for closure of the resolved-scale equations. With an eddy-viscosity prescription, the SFS fluxes are aligned with the resolved (filtered) strain rates and

are diagnosed with

$$\tau_{ij}^d = -2\nu_t S_{ij}, \quad (\text{A } 2)$$

where the eddy viscosity  $\nu_t$  needs to be modelled. Our particular SFS parameterization (Moeng 1984; Sullivan *et al.* 1994) utilizes

$$\nu_t = C_k l E_s^{1/2}, \quad (\text{A } 3)$$

where  $C_k$  is a modelling coefficient,  $l$  is a length scale, and the SFS energy  $E_s = \tau_{kk}/2$  evolves according to a prognostic TKE equation that includes large-scale advection, SFS production, buoyancy, diffusion, and dissipation, first proposed by Deardorff (1980). Viscous dissipation is parameterized by the Kolmogorov model

$$\epsilon = C_\epsilon \frac{E_s^{3/2}}{l}, \quad (\text{A } 4)$$

where  $C_\epsilon$  is another modelling coefficient. SFS buoyancy fluxes, which appear in the equations for resolved potential temperature  $\bar{\theta}$  and SFS TKE, are modelled with the gradient assumption

$$\tau_{\theta i} = \frac{\nu_t}{Pr_t} \frac{\partial \bar{\theta}}{\partial x_i}, \quad (\text{A } 5)$$

where the turbulent Prandtl number

$$Pr_t = \frac{\Delta_f}{\Delta_f + 2l}. \quad (\text{A } 6)$$

In regions of unstable stratification ( $\partial \bar{\theta} / \partial z < 0$ ) the length scale is set equal to the LES filter width:

$$l = \Delta_f, \quad (\text{A } 7)$$

while for stable stratification ( $\partial \bar{\theta} / \partial z > 0$ )

$$l = C_l E_s^{1/2} \left( \frac{g}{\theta_o} \frac{\partial \bar{\theta}}{\partial z} \right)^{-1/2}, \quad (\text{A } 8)$$

with  $C_l = 0.76$ . Deardorff (1980) originally suggested the use of a stability-corrected length scale (A 8) to improve entrainment rate predictions of stratocumulus clouds but its appropriateness for PBL turbulence is unknown. While the above TKE model is the default implementation in our LES code, its structure and the numerical value of the coefficients have been adjusted to suit particular PBL flows (e.g. Moeng & Wyngaard 1988; Sullivan *et al.* 1994; Patton *et al.* 1998; Saiki *et al.* 2000).

The Smagorinsky model (and its variants) is the most widely used SFS model in neutral engineering flows (e.g. Meneveau & Katz 2000) and is often used in LES of the PBL with buoyancy corrections (e.g. Mason & Brown 1999). Hence, we also consider the classic Smagorinsky (1963) model in our evaluation:

$$\nu_t = (C_s l)^2 |S|, \quad (\text{A } 9)$$

where the magnitude of the strain rate tensor  $|S| = \sqrt{2S_{ij}S_{ij}}$ . A relationship between the Smagorinsky and TKE model coefficients can be obtained by considering a truncated form of the SFS TKE equation. If a balance between SFS production and dissipation is assumed (i.e. equilibrium flow with small advection, diffusion, and buoyancy)

$$-\tau_{ij} S_{ij} = \epsilon, \quad (\text{A } 10)$$

and (A 2), (A 3), and (A 4) are substituted into (A 10) then the relationship between model coefficients becomes

$$C_s^2 = C_k \left( \frac{C_k}{C_\epsilon} \right)^{1/2}. \quad (\text{A } 11)$$

In a pioneering study, Lilly (1967) obtained estimates of the SFS model coefficients  $C_\epsilon$ ,  $C_k$ , and  $C_s$  under idealized conditions for a sharp spectral cutoff filter. In practice, however, non-sharp filters are frequently used and thus it is worthwhile to estimate the SFS model coefficients for other filter shapes. Our analysis follows Lilly (1967) and we adopt a Kolmogorov spectral form so that the LES filter scale always lies in the inertial range of the turbulence. For a general filter function  $G(k)$ , the SFS energy  $E_s$  is obtained from the energy spectrum function  $E(k)$  by integrating over all scalar wavenumbers  $k$ :

$$E_s = \int_0^\infty [1 - G^2(k)] E(k) dk. \quad (\text{A } 12)$$

Given the spectrum  $E = K_o \epsilon^{2/3} k^{-5/3}$  with the dissipation  $\epsilon$  modelled by (A 4) and a constant length scale  $l = \Delta_f$ , (A 12) reduces to

$$C_\epsilon = (K_o I_o)^{-3/2}, \quad (\text{A } 13)$$

where  $I_o$  is computed from

$$I_o = \int_0^\infty [1 - G^2(\beta)] \beta^{-5/3} d\beta. \quad (\text{A } 14)$$

The dimensionless wavenumber  $\beta = \Delta_f k$ .

An expression for the eddy-viscosity coefficient  $C_k$  is similarly obtained by assuming a balance between the average SFS production and dissipation,  $\langle -\tau_{ij} S_{ij} \rangle = \langle \epsilon \rangle$  and using an isotropic form for the energy spectrum (Lilly 1967; Moeng & Wyngaard 1988; Pope 2000, p. 579). The general relationship for the TKE eddy-viscosity coefficient is

$$C_k = \frac{C_\epsilon^{1/3}}{K_o I_1}, \quad (\text{A } 15)$$

where

$$I_1 = \int_0^\infty \beta^{1/3} G^2(\beta) d\beta. \quad (\text{A } 16)$$

$C_\epsilon$ ,  $C_k$ , and  $C_s$  are computed from (A 13), (A 15), and (A 11), respectively, with  $I_o$  and  $I_1$  containing the filter dependence.

We consider two filters that are used in practice; a sharp cutoff filter defined as:

$$G(\beta) = \begin{cases} 1, & 0 < \beta < \pi \\ 0, & \pi \leq \beta < \infty; \end{cases} \quad (\text{A } 17)$$

and a Gaussian filter

$$G(\beta) = \exp(-\beta^2/24). \quad (\text{A } 18)$$

The integrals  $I_o$  and  $I_1$  can be evaluated in closed form for the sharp spectral cutoff filter (Lilly 1967; Moeng & Wyngaard 1988). In the case of Gaussian filtering, a closed-form expression for  $I_1$  exists, while a numerical quadrature is used to evaluate  $I_o$ . The values of the SFS model coefficients and the integrals ( $I_o$ ,  $I_1$ ) for these two filters are given in table 2. The important aspect to notice is that the dissipation and eddy-viscosity coefficients ( $C_\epsilon$ ,  $C_k$ ) are filter dependent: they are lower for Gaussian

---

Filter	$C_\epsilon$	$C_k$	$C_s$	$I_o$	$I_1$
Sharp cutoff	0.93	0.094	0.173	$3\pi^{-2/3}/2$	$3\pi^{4/3}/2$
Gaussian	0.66	0.081	0.168	0.874	7.10

---

TABLE 2. SFS model coefficients for different filters with  $K_o = 1.5$ .

filtering than for the sharp spectral cutoff filter. However, the Smagorinsky coefficient  $C_s$  remains relatively unchanged because of compensating changes in  $C_k$  and  $C_\epsilon$ .

## REFERENCES

- ANTONIA, R. A. & KIM, J. 1994 A numerical study of local isotropy of turbulence. *Phys. Fluids* **6**, 834–841.
- BARDINA, J., FERZIGER, J. H. & REYNOLDS, W. C. 1983 Improved turbulence models based on large eddy simulation of homogeneous, incompressible, turbulent flows. *Rep. TF-19*. Thermosciences Division, Dept. Mechanical Engng, Stanford University.
- CANUTO, V. M. & CHENG, Y. 1997 Determination of the Smagorinsky-Lilly constant  $C_s$ . *Phys. Fluids* **9**, 1368–1378.
- DEARDORFF, J. W. 1970 A numerical study of three-dimensional turbulent channel flow at large Reynolds numbers. *J. Fluid Mech.* **41**, 453–480.
- DEARDORFF, J. W. 1973 The use of subgrid transport equations in a three-dimensional model of atmospheric turbulence. *Trans. ASME: J. Fluids Engng* **95**, 429–438.
- DEARDORFF, J. W. 1980 Stratocumulus-capped mixed layers derived from a three-dimensional model. *Boundary-layer Met.* **18**, 495–527.
- DUBRULLE, B., LAVAL, J.-P., SULLIVAN, P. P. & WERNE, J. 2002 A new dynamical subgrid model for the planetary surface layer. I. The model and *a priori* tests. *J. Atmos. Sci.* **59**, 857–872.
- GERMANO, M. 1986 A proposal for a redefinition of the turbulent stresses in the filtered Navier–Stokes equations. *Phys. Fluids* **29**, 2323–2324.
- GERMANO, M., PIOMELLI, U., MOIN, P. & CABOT, W. H. 1991 A dynamic subgrid-scale eddy viscosity. *Phys. Fluids A* **3**, 1760–1765.
- GHOSAL, S. & MOIN, P. 1995 The basic equations for the large eddy simulation of turbulent flows in complex geometry. *J. Comput. Phys.* **118**, 24–37.
- HÄRTEL, C. & KLEISER, L. 1997 Galilean invariance and filtering dependence of near-wall grid-scale/subgrid-scale interactions in large-eddy simulation. *Phys. Fluids* **9**, 473–475.
- HORIUTI, K. 1989 The role of the Bardina model in large eddy simulation of turbulent channel flow. *Phys. Fluids A* **1**, 426–428.
- HORST, T. W., KLEISSL, J., LENSCHOW, D. H., MENEVEAU, C., MOENG, C.-H., PARLANGE, M. B., SULLIVAN, P. P. & WEIL, J. C. 2002 Field Measurements of spatially-filtered turbulence in the atmospheric surface layer. *15th Symp. on Boundary Layers and Turbulence, University of Wageningen, the Netherlands*, pp. 436–439. Am. Met. Soc.
- HUNT, J. C. R., STRETCH, D. D. & BRITTER, R. E. 1988 Length scales in stably stratified turbulent flows and their use in turbulence models. In *Stably Stratified Flows and Dense Gas Dynamics* (ed. J. S. Puttock). Clarendon.
- JOHANSSON, C., SMEDMAN, A., HÖGSTROM, U., BRASSEUR, J. G. & KHANNA, S. 2001 Critical test of the validity of Monin-Obukhov similarity theory during convective conditions. *J. Atmos. Sci.* **58**, 1549–1566.
- JUNEJA, A. & BRASSEUR, J. G. 1999 Characteristics of subgrid-resolved-scale dynamics in anisotropic turbulence, with application to rough-wall boundary layers. *Phys. Fluids* **11**, 3054–3068.
- KAIMAL, J. C., EVERSOLE, R. A., LENSCHOW, D. H., STANKOV, B. B., KAHN, P. H. & BUSINGER, J. A. 1982 Spectral characteristics of the convective boundary layer over uneven terrain. *J. Atmos. Sci.* **39**, 1098–1114.
- KAIMAL, J. C. & FINNIGAN, J. J. 1994 *Atmospheric Boundary Layer Flows*. Oxford University Press.
- KAIMAL, J. C., WYNGAARD, J. C., HAUGEN, D. A., COTÉ, O. R., IZUMI, Y., CAUGHEY, S. J. & READINGS, C. J. 1976 Turbulence structure in the convective boundary layer. *J. Atmos. Sci.* **33**, 2152–2169.

- KAIMAL, J. C., WYNGAARD, J. C., IZUMI, Y. & COTÉ, O. R. 1972 Spectral characteristics of surface layer turbulence. *Q. J. R. Met. Soc.* **98**, 563–589.
- KALTENBACH, H.-J. 1997 Cell aspect ratio dependence of anisotropy measures for resolved and subgrid scale stresses. *J. Comput. Phys.* **136**, 399–410.
- KATOPODES, F. V., STREET, R. L. & FERZIGER, J. H. 2000 A theory for the subfilter-scale model in large-eddy simulation. *Environmental Fluid Mechanics Laboratory Tech. Rep.* 2000-K1. Stanford University.
- KHANA, S. & BRASSEUR, J. 1997 Analysis of Monin-Obukhov similarity from large-eddy simulation. *J. Fluid Mech.* **345**, 251–286.
- KIMURA, Y. & HERRING, J. R. 1996 Diffusion in stably stratified turbulence. *J. Fluid Mech.* **328**, 253–269.
- LANCZOS, C. 1956 *Applied Analysis*. Prentice Hall.
- LEITH, C. 1990 Stochastic backscatter in a subgrid-scale model: Plane shear mixing layer. *Phys. Fluids* **2**, 297–299.
- LEONARD, A. 1974 Energy cascade in large eddy simulations of turbulent fluid flows. *Adv. Geophys.* **18**, 237–248.
- LEONARD, A. 1997 Large-eddy simulation of chaotic convection and beyond. *AIAA Paper* 97-0204.
- LILLY, D. K. 1967 The representation of small-scale turbulence in numerical simulation experiments. In *Proc. IBM Scientific Computing Symp. on Environmental Sciences* (ed. H. H. Goldstine), pp. 195–210. Yorktown Heights, NY: IBM.
- LIU, S., MENEVEAU, C. & KATZ, J. 1994 On the properties of similarity subgrid-scale models as deduced from measurements in a turbulent jet. *J. Fluid Mech.* **275**, 83–119.
- LUMLEY, J. L. 1978 The computational modelling of turbulent flows. *Adv. Appl. Mech.* **18**, 123–176.
- MASON, P. J. & BROWN, A. R. 1999 On subgrid models and filter operations in large-eddy simulations. *J. Atmos. Sci.* **56**, 2101–2114.
- MASON, P. J. & CALLEN, N. S. 1986 On the magnitude of the subgrid-scale eddy coefficient in large-eddy simulations of turbulent channel flow. *J. Fluid Mech.* **162**, 439–462.
- MASON, P. J. & THOMSON, D. J. 1992 Stochastic backscatter in large-eddy simulations of boundary layers. *J. Fluid Mech.* **242**, 51–78.
- MENEVEAU, C. & KATZ, J. 2000 Scale-invariance and turbulence models for large-eddy simulations. *Annu. Rev. Fluid Mech.* **32**, 1–32.
- MENEVEAU, C. & LUND, T. S. 1997 The dynamic Smagorinsky model and scale-dependent coefficients in the viscous range of turbulence. *Phys. Fluids* **9**, 3932–3934.
- MOENG, C.-H. 1984 A large-eddy simulation model for the study of planetary boundary-layer turbulence. *J. Atmos. Sci.* **41**, 2052–2062.
- MOENG, C.-H. & SULLIVAN, P. P. 1994 A comparison of shear and buoyancy driven planetary-boundary-layer flows. *J. Atmos. Sci.* **51**, 999–1022.
- MOENG, C.-H. & WYNGAARD, J. C. 1988 Spectral analysis of large-eddy simulations of the convective boundary layer. *J. Atmos. Sci.* **45**, 3573–3587.
- MOIN, P. & KIM, J. 1982 Numerical investigation of turbulent channel flow. *J. Fluid Mech.* **118**, 341–377.
- NIEUWSTADT, F. T. M., MASON, P. J., MOENG, C.-H. & SCHUMANN, U. 1993 Large-eddy simulation of the convective boundary layer: A comparison of four computer codes. In *Turbulent Shear Flows 8* (ed. F. Durst *et al.*). Springer.
- PANOFSKY, H. & DUTTON, J. 1984 *Atmospheric Turbulence: Models and Methods for Engineering Applications*. Wiley.
- PATTON, E. G., SHAW, R. H., JUDD, M. J. & RAUPACH, M. R. 1998 Large-eddy simulation of windbreak flow. *Boundary-Layer Met.* **87**, 275–306.
- PELTIER, L. J., WYNGAARD, J. C., KHANNA, S. & BRASSEUR, J. 1996 Spectra in the unstable surface layer. *J. Atmos. Sci.* **53**, 49–61.
- PIOMELLI, U., CABOT, W. H., MOIN, P. & LEE, S. 1991 Subgrid-scale backscatter in turbulent and transitional flows. *Phys. Fluids* **3**, 1766–1771.
- PIOMELLI, U., YU, Y. & ADRIAN, R. J. 1996 Subgrid-scale energy transfer and near-wall turbulence structure. *Phys. Fluids* **8**, 215–224.
- POPE, S. B. 2000 *Turbulent Flows*. Cambridge University Press.

- PORTÉ-AGEL, F., PARLANGE, M. B., MENEVEAU, C. & EICHINGER, W. E. 2001 A priori field study of the subgrid-scale heat fluxes and dissipation in the atmospheric surface layer. *J. Atmos. Sci.* **58**, 2673–2698.
- ROGALLO, R. S. & MOIN, P. 1984 Numerical simulation of turbulent flows. *Annu. Rev. of Fluid Mech.* **16**, 99–137.
- RILEY, J. J. & LELONG, M.-P. 2000 Fluid motions in the presence of strong stable stratification. *Annu. Rev. Fluid Mech.* **32**, 613–657.
- SAIKI, E. M., MOENG, C.-H. & SULLIVAN, P. P. 2000 Large eddy simulation of the stably stratified planetary boundary layer. *Boundary-Layer Met.* **95**, 1–30.
- SCHUMANN, U. 1991. Subgrid length scale for large eddy simulation of stratified turbulence. *Theor. Comput. Fluid Dyn.* **2**, 279.
- SCHUMANN, U. 1995 Stochastic backscatter of turbulence energy and scalar variance by random subgrid-scale fluxes. *Proc. R. Soc. Lond. A* **451**, 293.
- SCOTTI, A., MENEVEAU, C. & FATICA, M. 1997 Dynamic smagorinsky model on anisotropic grids. *Phys. Fluids* **9**, 1856–1858.
- SCOTTI, A., MENEVEAU, C. & LILLY, D. K. 1993 Generalized smagorinsky model for anisotropic grids. *Phys. Fluids A* **5**, 2306–2308.
- SMAGORINSKY, J. 1963 General circulation experiments with the primitive equations. I. The basic experiment. *Mon. Wea. Rev.* **91**, 99–164.
- SPALART, P. R., JOU, W.-H., STRELETS, M. & ALLMARAS, S. R. 1997 Comments on the feasibility of LES for wings, and on a hybrid RANS/LES approach. In *Advances in DNS/LES: First AFOSR Intl Conf. on DNS/LES, Aug. 4–8, 1997, Ruston, Louisiana* (ed. C. Liu & Z. Liu). Greyden Press, Columbus, OH.
- SPEZIALE, C. G. 1985 Galilean invariance of subgrid-scale stress models in the large-eddy simulation of turbulence. *J. Fluid Mech.* **156**, 55–62.
- STEVENS, B., MOENG, C.-H. & SULLIVAN, P. P. 1999 Large-eddy simulation of radiatively driven convection: Sensitivities to the representation of small scales. *J. Atmos. Sci.* **56**, 3963–3984.
- STOLZ, S., ADAMS, N. A. & KLEISER, L. 2001 An approximate deconvolution model for large-eddy simulation with application to incompressible wall-bounded flows. *Phys. Fluids* **13**, 997–1015.
- SULLIVAN, P. P., MCWILLIAMS, J. C. & MOENG, C.-H. 1996 A grid nesting method for large-eddy simulation of planetary boundary layer flows. *Boundary-Layer Met.* **80**, 167–202.
- SULLIVAN, P. P., MCWILLIAMS, J. C. & MOENG, C.-H. 1994 A subgrid-scale model for large-eddy simulation of planetary boundary-layer flows. *Boundary-Layer Met.* **71**, 247–276.
- TAO, B., KATZ, J. & MENEVEAU, C. 2000 Geometry and scale relationships in high Reynolds number turbulence determined from three-dimensional holographic velocimetry. *Phys. Fluids* **12**, 941–944.
- TONG, C., WYNGAARD, J. C. & BRASSEUR, J. G. 1999 Experimental study of the subgrid-scale stresses in the atmospheric surface layer. *J. Atmos. Sci.* **56**, 2277–2292.
- TONG, C., WYNGAARD, J. C., KHANNA, S. & BRASSEUR, J. G. 1998 Resolvable- and subgrid-scale measurement in the atmospheric surface layer: Technique and issues. *J. Atmos. Sci.* **55**, 3114–3126.
- VREMAN, B., GEURTS, B. & KUERTEN, H. 1997 Large-eddy simulation of the turbulent mixing layer. *J. Fluid Mech.* **339**, 357–390.
- WINCKELMANS, G., WRAY, A., VASILYEV, O. & JEANMART, H. 2001 Explicit-filtering large eddy simulation using the tensor-diffusivity model supplemented by a dynamic Smagorinsky term. *Phys. Fluids* **13**, 1385–1403.
- YOSHIZAWA, A. 1998 *Hydrodynamic and Magnetohydrodynamic Turbulent Flows: Modelling and Statistical Theory*. Kluwer.
- ZHOU, Y., BRASSEUR, J. G. & JUNEJA, A. 2001 A resolvable subfilter-scale model specific to large-eddy simulation of under-resolved turbulence. *Phys. Fluids* **13**, 2602–2610.